



**HAL**  
open science

## 5-Hydroxymethylfurfural Oxidation to 2,5-Furandicarboxylic Acid on Noble Metal-Free Nanocrystalline Mixed Oxide Catalysts

Atif Emre Demet, Olinda Gimello, Rossella Arletti, Nathalie Tanchoux,  
Moulay Tahar Sougrati, Lorenzo Stievano, Françoise Quignard, Gabriele  
Centi, Siglinda Perathoner, Francesco Di Renzo

► **To cite this version:**

Atif Emre Demet, Olinda Gimello, Rossella Arletti, Nathalie Tanchoux, Moulay Tahar Sougrati, et al.. 5-Hydroxymethylfurfural Oxidation to 2,5-Furandicarboxylic Acid on Noble Metal-Free Nanocrystalline Mixed Oxide Catalysts. *Catalysts*, 2022, 12 (8), pp.814. 10.3390/catal12080814. hal-03762718

**HAL Id: hal-03762718**

**<https://cnrs.hal.science/hal-03762718>**

Submitted on 28 Aug 2022

**HAL** is a multi-disciplinary open access archive for the deposit and dissemination of scientific research documents, whether they are published or not. The documents may come from teaching and research institutions in France or abroad, or from public or private research centers.

L'archive ouverte pluridisciplinaire **HAL**, est destinée au dépôt et à la diffusion de documents scientifiques de niveau recherche, publiés ou non, émanant des établissements d'enseignement et de recherche français ou étrangers, des laboratoires publics ou privés.

## Article

# 5-Hydroxymethylfurfural Oxidation to 2,5-Furandicarboxylic Acid on Noble Metal-Free Nanocrystalline Mixed Oxide Catalysts

Atif Emre Demet <sup>1,2,3</sup>, Olinda Gimello <sup>2</sup>, Rossella Arletti <sup>4</sup>, Nathalie Tanchoux <sup>2</sup>, Moulay Tahar Sougrati <sup>2</sup>, Lorenzo Stievano <sup>2</sup>, Françoise Quignard <sup>2</sup>, Gabriele Centi <sup>5</sup>, Siglinda Perathoner <sup>1</sup> and Francesco Di Renzo <sup>2,\*</sup>

<sup>1</sup> Department ChiBioFarAm, Università di Messina, 98166 Messina, Italy; atifemredemet@gmail.com (A.E.D.); perathon@unime.it (S.P.)

<sup>2</sup> ICGM, Université de Montpellier, CNRS, ENSCM, 34090 Montpellier, France; olinda.gimello@enscm.fr (O.G.); nathalie.tanchoux@enscm.fr (N.T.); moulay-tahar.sougrati@umontpellier.fr (M.T.S.); lorenzo.stievano@umontpellier.fr (L.S.); quignard@enscm.fr (F.Q.)

<sup>3</sup> Energy System Engineering, Necmettin Erbakan University, Köyceğiz Mah. Demeç Sok. No:42/A Meram, Konya 42090, Turkey

<sup>4</sup> Department Chemical and Geological Sciences, Università di Modena e Reggio Emilia, 41125 Modena, Italy; rossella.arletti@unimore.it

<sup>5</sup> MIFT, Università di Messina, 98166 Messina, Italy; centi@unime.it

\* Correspondence: francesco.di-renzo@umontpellier.fr; Tel.: +33-607508148

**Citation:** Demet, A.E.; Gimello, O.; Arletti, R.; Tanchoux, N.; Sougrati, M.T.; Stievano, L.; Quignard, F.; Centi, G.; Perathoner, S.; Di Renzo, F. 5-Hydroxymethylfurfural Oxidation to 2,5-Furandicarboxylic Acid on Noble Metal-Free Nanocrystalline Mixed Oxide Catalysts. *Catalysts* **2022**, *12*, 814. <https://doi.org/10.3390/catal12080814>

Academic Editors: Karine De Oliveira Vigier, Mickael Capron, Christophe Len

Received: 19 June 2022

Accepted: 22 July 2022

Published: 25 July 2022

**Publisher's Note:** MDPI stays neutral with regard to jurisdictional claims in published maps and institutional affiliations.



**Copyright:** © 2022 by the authors. Licensee MDPI, Basel, Switzerland. This article is an open access article distributed under the terms and conditions of the Creative Commons Attribution (CC BY) license (<https://creativecommons.org/licenses/by/4.0/>).

**Abstract:** Noble metal-free catalysts based on earth-abundant and inexpensive mixed oxides are active catalysts of all steps of the reaction cascade leading from 5-hydroxymethylfurfural (HMF) to 2,5-furandicarboxylic acid (FDCA) using tert-butyl hydroperoxide (TBHP) as oxidation agent. Catalysts covering the whole range of composition in the Cu-Mn and Co-Fe series have been prepared and characterised. The nature and composition of the catalyst strongly affect conversion and selectivity. The distribution of products indicates that radical-type oxygen species, deriving from the activation of TBHP, play a determining role in the reaction. The early steps of reaction mainly follow the pattern expected for heterogeneous Fenton catalysts. Mixed oxide catalysts are the most effective in further oxidation steps, leading to the formation of FDCA, both in the Cu-Mn and Co-Fe systems. This behaviour can be related to the distribution of charge in the mixed oxides, suggesting a possible implication of the lattice oxygen in the last reaction steps. The results provide indications on how to optimize the reaction and minimize the formation of byproducts (humins and oligomers).

**Keywords:** noble metal-free catalysts; HMF; FDCA; renewable resource; cobalt-iron oxides; copper-manganese oxides; Mössbauer spectroscopy

## 1. Introduction

The synthesis of FDCA (2,5-furandicarboxylic acid) is at the center of a wide research effort as one of the most promising high-added-value biorefinery products [1]. FDCA, together with ethylene glycol, allows the production of PEF (polyethylene furanoate), a bio-based alternative to fossil-fuel-based PET (polyethylene terephthalate), one of the largest volume polymers [2]. Its catalytic synthesis from HMF (5-hydroxymethylfurfural), a platform molecule derived from renewable resources [3–5], is one of the main ways for the introduction of renewable feedstocks in polymer production [6,7].

The oxidation of HMF to FDCA is a complex cascade process involving several intermediates in parallel or successive reactions (Figure 1) [8]. The first step of the process can imply either the oxydehydrogenation of the alcohol group of HMF to aldehyde, forming 2,5-diformylfuran (DFF), or the oxidation of the carbonyl group to carboxylic acid into

5-hydroxymethyl-2-furancarboxylic acid (HMFCFA). The successive steps are the oxidation of a carbonyl group of DFF or the oxydehydrogenation of the alcohol group of HMFCFA, both reactions forming 5-formyl-2-furancarboxylic acid (FFCA), which is later oxidised to FDCA. This reaction mechanism, already quite complex from a kinetic point of view, can be further complexified by several reactions in competition with the oxidation to FDCA, such as the formation of maleic anhydride by oxydecarboxylation [9], the condensation to oligomers and humins [10,11], or the opening of the furanic ring by overoxidation [12–15].

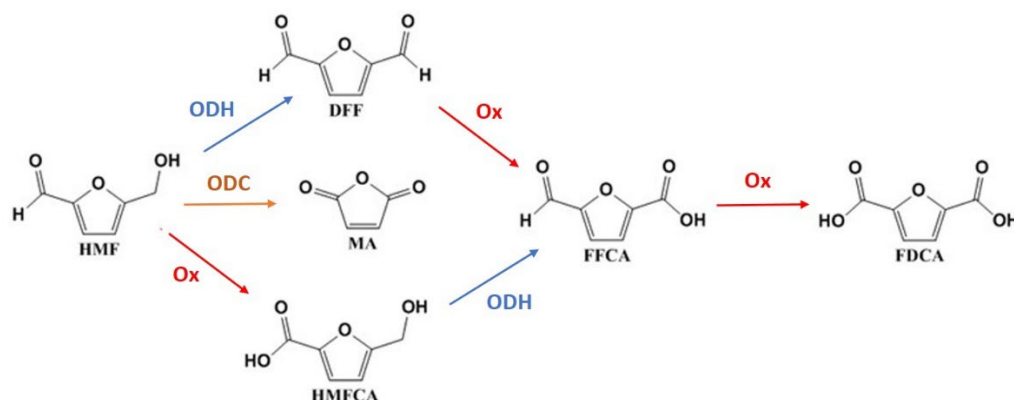


**Figure 1.** Consecutive-parallel reaction pathways in the oxidation of HMF to FDCA. ODH: oxydehydrogenation; ODC: oxydecarboxylation; Ox: aldehyde oxidation.

The largest majority of the catalysts proposed for this process are based on supported noble metals [16–20]: Pt [21–31], Pd or Pd-alloys [13,32–40], Au or gold-alloys [41–48], Ru [49–55], and Ag oxide [56–58]. A selection of literature results, presented in Table 1, provides some indication of the effectiveness of noble metal catalysts and on their different behaviours. The reaction is usually performed in water under an oxygen atmosphere. The availability of an oxidant depends on the solubility of oxygen. The time course of the reaction presents an initial phase of faster oxidation of HMF to FFCA through DFF or HMFCFA intermediates, followed by a phase of slower oxidation of FFCA to FDCA. The nature of the catalyst and the support affect the relative relevance of the two possible paths to FFCA, through either DFF or HMFCFA. Basic supports are nearly always used. Hydroxide supports especially affect the reaction pathway. DFF intermediates are mainly observed on Pt, Ru, and AuPd alloys on supports without structural hydroxide groups, like doped carbon or carbon nanotubes. HMFCFA is the main intermediate observed on hydroxide-supported catalysts and on Au, Pd, and Ag catalysts. It can be remarked that the observation of an intermediate, either DFF or HMFCFA, does not prove that FFCA is mostly formed through the most observed intermediate, which can just be accumulated by a very slow rate of reaction towards the final product.

**Table 1.** Selected literature results of base-free HMF oxidation on supported noble metal catalysts.

Catalyst	Oxidant	Solvent	T °C	Time h	Conversion Productivity			Selectivity %			Ref.
					HMF %	mmol g <sup>-1</sup> h <sup>-1</sup>	DFP	HMFCFA	FFCA	FDCA	
Pt (4.9%)/Mg-carbon	O <sub>2</sub> (0.5 MPa)	H <sub>2</sub> O	110	3	86	7.20	26	0	58	17	[24]
				17	100	1.48	0	0	100		
Pt (5%)/N-carbon	O <sub>2</sub> (1 MPa)	H <sub>2</sub> O	110	4	60	3.20	18	0	53	33	[23]
				12	99	1.06	0	0	98		
Pt (1%)/LDH	O <sub>2</sub> (40 mL/min)	H <sub>2</sub> O	95	2	74	2.60	0	0	54	31	[35]
				8	100	0.89	0	0	7	87	
Pt <sub>0.4</sub> Cu <sub>0.6</sub> (0.74%)/C	O <sub>2</sub> (1 MPa)	H <sub>2</sub> O	150	1	100	7.50	16	0	74	9	[31]
				6	100	1.25	0	0	99		
Pt <sub>0.8</sub> Pd <sub>0.2</sub> (1%)/LDH	O <sub>2</sub> (40 mL/min)	H <sub>2</sub> O	95	2	87	3.10	0	3	51	42	[35]
				8	100	0.89	0	0	1	99	
Pd (1%)/LDH	O <sub>2</sub> (40 mL/min)	H <sub>2</sub> O	95	2	91	3.20	0	20	44	16	[35]
				8	98	0.87	0	8	30	53	
Au (1%)/NiO	O <sub>2</sub> (1 MPa)	H <sub>2</sub> O	90	6	70	0.59	0	24	40	35	[47]
				20	74	0.18	0	21	30	48	
Au (1.92%)/LDH	O <sub>2</sub> flowing	H <sub>2</sub> O	95	3	97	1.20	0	53	8	37	[41]
				7	100	0.55	0	0	100		
Au <sub>0.5</sub> Pd <sub>0.5</sub> (1%)/CNT	O <sub>2</sub> (0.5 MPa)	H <sub>2</sub> O	90	2	68	2.24	19	0	53	23	[13]
				12	100	0.55	0	0	2	94	
Au <sub>0.67</sub> Pd <sub>0.33</sub> (1%)/NiO	O <sub>2</sub> (1 MPa)	H <sub>2</sub> O	90	2	76	1.93	2	7	57	33	[47]
				14	100	0.32	0	0	0	100	
Au <sub>0.56</sub> Pd <sub>0.44</sub> (2.75%)/La-LDH	O <sub>2</sub> (0.5 MPa)	H <sub>2</sub> O	120	0.5	86	17.20	3	45	23	27	[33]
				4	100	2.50	0	0	0	100	
Ru (5%)/C	O <sub>2</sub> (0.2 MPa)	H <sub>2</sub> O	120	1	86	4.30	14	0	75	0	[50]
				10	100	0.50	0	0	0	88	
Ru (2.4%)/LDH	O <sub>2</sub> (0.25 MPa)	H <sub>2</sub> O	140	2	98	4.30	11	56	n.a	28	[49]
				6	100	0.50	0	1	n.a	99	

CNT: carbon nanotubes; LDH: layered double hydroxide; n.a.: data not provided.

In a general way, the use of hydroxide supports significantly increased the rate of oxidation. This effect has been attributed to the nucleophilic addition of a surface hydroxide to the aldehyde group of HMF, allowing the formation of a gem-diol intermediate, which can be oxydehydrated to form the carboxylic group of HMFCFA [23,36]. A potential drawback of several layered double hydroxide (LDH) supports is the poor reusability, due to Mg leaching in the reaction solution [13,59]. The use of MgCaAl LDH or the incorporation of other basic oxides has been proposed to improve the reusability of the catalyst [33]. On the basis of this role of the hydroxide, it is not surprising that dissolved alkalis were widely used to sustain the activity of HMF oxidation catalysts [12,25,28,39,44,60–62]. Selected literature results are reported in Table 2.

**Table 2.** Selected literature results of base-assisted HMF oxidation in water on supported noble metal catalysts.

Catalyst	Oxidant	Base	T		Time Conversion Productivity			Selectivity %			Ref.
			°C	h	HMF %	mmol g <sup>-1</sup> h <sup>-1</sup>	DFF	HMFCFA	FFCA	FDCA	
Pt (20%)/C	O <sub>2</sub> (1 MPa)	NaOH/ HMF 20	50	1	99	10.20	0	31	15	47	[61]
				8	100	1.30	0	13	1	83	
Pt (3.4%) Bi (0.7%)/ TiO <sub>2</sub>	air (4 MPa)	Na <sub>2</sub> CO <sub>3</sub> / HMF 2	100	0.5	100	34.90	0	13	25	52	[28]
				4	100	4.35	0	0	0	99	
Au <sub>0.6</sub> Pt <sub>0.4</sub> (1%)/C	O <sub>2</sub> (0.3 MPa)	Na <sub>2</sub> CO <sub>3</sub> / HMF 2	60	2	100	5.10	n.a	38	n.a	62	[44]
				6	100	1.70	n.a	6	n.a	94	
Au (2.6%)-CeO <sub>2</sub>	air (1 MPa)	Na <sub>2</sub> OH/ HMF 4	65	1	100	19.80	0	98	0	1	[12]
				8	100	2.48	0	0	0	99	
Au (1.5%)-CeO <sub>2</sub>	O <sub>2</sub> (1 MPa)	Na <sub>2</sub> OH/ HMF 4	95	0.5	100	15.20	0	1.7	67	30	[62]
				3	100	2.50	0	0	1.4	98	
Au <sub>0.86</sub> Pd <sub>0.14</sub> (1.5%)/ TiO <sub>2</sub>	O <sub>2</sub> (1 MPa)	Na <sub>2</sub> OH/ HMF 2	70	0.5	100	16.30	0	43	4	52	[39]
				4	100	2.00	0	13	4	85	
Au <sub>0.5</sub> Pd <sub>0.5</sub> (2%)/ZOC	O <sub>2</sub> (0.3 MPa)	Na <sub>2</sub> HCO <sub>3</sub> / HMF 4	80	0.5	74	19.50	traces	25	55	19	[32]
				4	100	3.30	traces	0	0	100	
Au <sub>0.5</sub> Cu <sub>0.5</sub> (1.5%)/ TiO <sub>2</sub>	O <sub>2</sub> (1 MPa)	Na <sub>2</sub> OH/ HMF 4	95	1	100	11.50	n.a.	90	0	9	[60]
				4	100	2.90	n.a.	2	0	98	

ZOC: Zn hydroxycarbonate; n.a.: data not provided.

The use of a dissolved base has clearly brought an increase in productivity. The absence of detected DFF indicates that the aldehyde oxidation reaction Ox1 has prevailed on the alcohol oxydehydrogenation ODH1 (see Figure 1). Despite the observed increase in productivity, the use of alkaline solutions requires special care in order to balance the effects of the oxidation catalyst with the base-catalysed degradation of HMF, leading to ring-opening and condensation products, with a significant worsening of the carbon balance [29,60,61]. The base-induced Cannizzaro disproportionation of aldehydes to alcohols and acids can introduce reaction pathways in competition with oxidation, with the formation of BHMF (2,5-bis(hydroxymethyl)furan) and HMFCFA by disproportionation of HMF [63], the formation of FFCA and HMF by disproportionation of DFF, or the disproportionation of FFCA and HMF to FDCA and BHMF [39]. The esterification of aldehyde groups by Tishchenko coupling [64] can contribute to the formation of condensation products by a pathway different from the acid-catalysed aldol condensation to humins [10,65]. The realisation of the superposition of so different reaction pathways has relegated several interpretations of the kinetics of HMF oxidation to obsolescence.

The intrinsic reactivity of the substrate and the different possible reaction pathways under comparable reaction conditions question the specific role of the catalyst in the reaction mechanism, for example, the reactivity of surface oxygens as Me-OH sites as indicated by Davis et al. [42], or the specific activation of the reactants over the metal surface [33,58]. An alternative interpretation is based on the generation of the peroxo species by oxygen activation (which is less dependent on the nature of the noble metal particles), these species being then responsible for the catalytic transformation. This second interpretation is supported by some studies which use i) H<sub>2</sub>O<sub>2</sub> or organic peroxides as the oxidant [15,66] or ii) typical systems for homogeneous catalytic oxidation in the liquid phase (Co/Mn/Br catalyst) [67–70], where a radical mechanism is prevailing.

Understanding whether a radical-type mechanism activated from the generation of a peroxo-type oxygen species is present is a relevant question not only from a fundamental perspective but also for the possible development of novel, noble-metal free, catalysts for this reaction. There are, in fact, various motivations to develop this type of catalyst,

the main one being related to the prevention of the use of critical and expensive raw materials (such as noble metals) to develop environmentally friendly catalysts, an aspect particularly relevant in the production of bio-based chemicals where societal and environmental impacts are determining factors. This has motivated the existing studies on catalysts for FDCA synthesis not containing noble metals. However, some of them contain other critical raw materials such as cerium [12,62,71,72]. A limited number of studies were based on mixed oxides of widely available transition metals such as Mn, Fe, Co, or Cu [73–76]. Some selected literature results are reported in Table 3. The productivity of mixed oxide systems was largely comparable with the results obtained on supported noble metal catalysts in the absence of bases (Table 1). Transition metals were also incorporated in porous matrices [77,78], and especially high productivity was measured on very low-density porous organic polymers or graphene, which could require further support for scaled-up use [79,80].

**Table 3.** Selected literature results of HMF oxidation on non-noble metal catalysts.

Catalyst	Oxidant	Solvent	T	Time	Conversion	Productivity	Selectivity %			Ref.	
			°C	h	HMF %	mmol g <sup>-1</sup> h <sup>-1</sup>	DFE	HMFC	FFCA		FDCA
Co (7%)O <sub>x</sub> /α-Fe <sub>3</sub> O <sub>4</sub>	TBHP/ HMF 7	DMSO	80	2	39	1.08	33	12	0	51	[73]
				12	97	0.45	8	0	70		
	O <sub>2</sub> 20 mL/min	DMSO	80	12	13	0.06	50	0	0	32	
Cu (2.6%)-MnO <sub>2</sub>	TBHP/ HMF 65	TBA	80	1	39	1.08	13	0	57	28	[81]
				12	99	0.41	0.4	0	3	96	
	O <sub>2</sub> (0.1 MPa)	TBA	80	12	57	0.24	73	0	24	3	
CuMn <sub>2</sub> O <sub>4</sub>	TBHP/ HMF 15	CH <sub>3</sub> CN	80	4	100	5	8	8	55	29	[76]
				14	100	1.43	0	0	3	95	
Co (0.12%)-Py-resin	TBHP/ HMF 9	CH <sub>3</sub> CN	110	3	40	1.48	51	3	n.a	39	[77]
				24	78	0.36	15	2	n.a	78	
FeNP@NH <sub>2</sub> -SBA-15	O <sub>2</sub> (0.6 MPa)	H <sub>2</sub> O	120	6	86	2.4	0	37	14	47	[78]
				14	100	1.2	0	5	5	88	
Fe <sup>3+</sup> (0.015%)/POP	O <sub>2</sub> (1 MPa)	H <sub>2</sub> O	100	2	85	75	42	n.a	17	42	[79]
				10	100	26	3	n.a	3	85	
Cu (0.62%)/N-graphene	TBHP/ HMF 8	CH <sub>3</sub> CN	70	2	100	25	4	3	82	7	[80]
				24	100	2.1	0	0	30	60	

TBA: tert-butyl alcohol; TBHP: tert-butyl hydroperoxide; DMSO: dimethylsulfoxide; Py-resin: porphyrin on Merrifield resin; POP: porphyrin porous organic polymer; n.a.: data not provided.

Tert-butyl hydroperoxide (TBHP) was extensively used as the oxidant, providing higher oxidation yields than molecular oxygen [73,75,81], essentially due to the limited solubility of the latter. However, it was observed that TBHP could easily lead to the degradation and condensation of furanic compounds [82]. In several cases, also on this kind of catalyst, dissolved bases were used to foster the aldehyde oxidation [83,84].

The performances of the catalysts should still be improved. A better understanding of the mechanism and the role of the catalysts, innovative processes, and the direct injection of energy into the reaction system [54,61,85–87], can enhance selectivity and productivity. Another motivation to develop novel catalysts for HMF oxidation derives from an aspect that is not extensively investigated in the literature but instead is a critical question from an industrial perspective: the formation of products of poly-condensation during the liquid phase catalytic oxidation of HMF to FDCA. These products are difficult to analyse and thus they are often not considered in reporting the catalytic performances, especially when a careful carbon balance is not considered. However, in the industrial process, they

represent a major problem, because they are responsible for carbon loss and catalyst deactivation by fouling. These products, in addition to humins formed by acid-catalysed reactions followed by aldol addition and condensation [10], likely derive from radical-type reactions and it is important to understand the role of these reactions in the FDCA synthesis. Limiting these reactions is thus both relevant from the environmental perspective (to limit waste products) and to improve the stability of the catalyst.

In order to obtain information on these aspects and develop environmentally friendly catalysts, this work will investigate noble-metal-free mixed spinels of the Cu-Mn and Co-Fe series, not yet extensively investigated in the HMF oxidation to FDCA. Tert-butyl hydroperoxide is used as an oxidant because the aim is to understand the role of the peroxo species in the reaction mechanism. The comparison of the behaviour in the two series of spinel-type catalysts, with respect to their structural and redox characteristics, provides indications regarding the role of the radical-type species in the different steps of the reaction network. Together with the analysis of the effect of the reaction conditions, it is also possible to obtain an indication of how to minimize side reactions and maximize FDCA formation.

## 2. Results

### 2.1. Characterisation of Catalysts

#### 2.1.1. Copper-Manganese Oxides

Cu-Mn catalysts in the field of the atomic ratio Mn/(Cu + Mn) between 0 and 1 were prepared by coprecipitation and were calcined at 450 °C. The X-ray diffraction patterns of the catalysts are reported in Figure 2, the samples being called by their cation percent atomic ratio, for instance, Mn33Cu67. The formation of solid solutions with an extended field of continuous variation of composition is not favoured in the copper-manganese system [88]. The phase ratios observed for different global compositions of the samples are reported in Table S1. In the sample Cu100, the only observed phase is CuO tenorite. For Cu67Mn33 and Cu50Mn50, the phases observed are CuO and a cubic spinel. The increase of the manganese content brings about an increase in the fraction of spinel until the cubic spinel is the only observed phase for the sample Cu33Mn67. The phases observed in Mn100 are tetragonal haussmannite  $Mn_3O_4$  and  $Mn_5O_8$ .

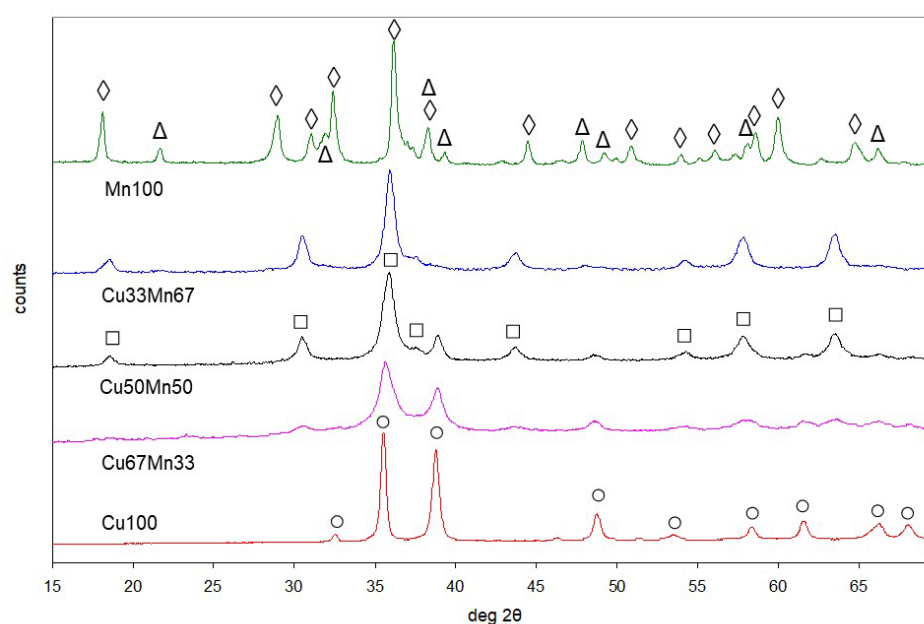


**Figure 2.** Powder XRD patterns of the Cu-Mn catalysts. CuO tenorite (○), cubic spinel (□),  $Mn_3O_4$  haussmannite (◇),  $Mn_5O_8$  (Δ).

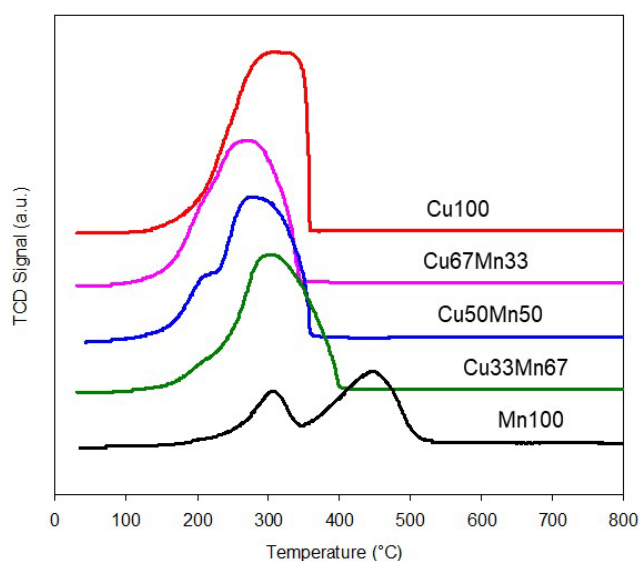
It is worth recalling that the cation distribution in copper-manganese spinels represents a special case of internal redox equilibrium between  $\text{Cu}^{\text{tet}} + \text{Mn}^{\text{oct}}$  and  $\text{Mn}^{\text{tet}} + \text{Cu}^{\text{oct}}$  [89]. This equilibrium is shifted as a function of the Mn/Cu ratio and copper becomes virtually completely oxidized to  $\text{Cu}^{2+}$  for Mn/Cu ratios lower than 1 [88,90]. However, copper-rich samples retain a significant amount of  $\text{Mn}^{4+}$  along  $\text{Mn}^{3+}$ , which will correspond to the creation of cation defects in the spinel structure [90,91]. The cell parameter of spinel, reported in Table 4, increases with manganese content but the less-than-expected increase corresponds to the presence of cation defects [92,93].

**Table 4.** Textural characterisation and spinel crystallographic data of Cu-Mn oxide catalysts.

Catalyst	S(BET)/m <sup>2</sup> g <sup>-1</sup>	Grain Size/nm			Spinel Cell/Å
		CuO	Spinel	Mn <sub>3</sub> O <sub>4</sub> Mn <sub>5</sub> O <sub>8</sub>	
Cu100	11	38			
Cu67Mn33	106	11	11		8.286 (4)
Cu50Mn50	75	15	14		8.290 (0)
Cu33Mn67	51		15		8.291 (4)
Mn100	24			22 25	

The surface area and grain size of the Cu-Mn samples are reported in Table 4. Further data from N<sub>2</sub> sorption are reported in Table S2 and Figure S1. In this system, the mixed oxides present a higher surface area than the copper and manganese end-terms. However, the surface area significantly varies with the composition of the oxides. The surface area features a maximum of more than 100 m<sup>2</sup> g<sup>-1</sup> for Cu67Mn33 and steadily decreases for higher Mn contents. It is remarkable that the grain size of tenorite is much smaller in the mixed samples than for CuO crystallised alone in Cu100 and is comparable to the grain size of spinel. This strongly suggests that the presence of foreign cations increases the ratio between nucleation and growth rates of the oxide. The grain size of each phase of the mixed samples slightly increases with the Mn content.

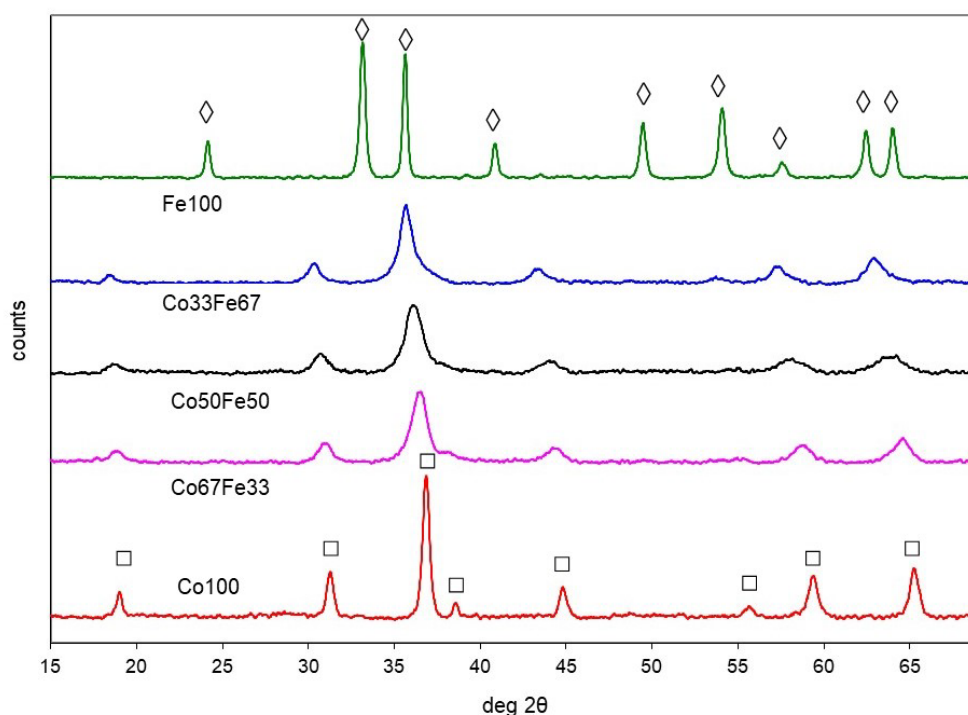
The TPR profiles of the Cu-Mn catalysts are reported in Figure 3. The consumption of H<sub>2</sub> in the tests is reported in Table S3. The reduction of the CuO sample to metallic Cu begins at nearly 125 °C and is completed at 365 °C after a highly skewed peak with a maximum of 310 °C. In the case of the mixed Cu-Mn samples, the onset of the reduction is always observed at nearly 125 °C and develops into a shoulder at about 220 °C, with intensities decreasing as the copper content decreases. This initial reduction signal probably corresponds to the fast reduction of small-crystal CuO (see Table 4). The main reduction peak corresponds to the reductive decomposition of spinel. The maximum temperature of the main peak of the reduction of spinel increases from 275 to 305 °C at the increase of the manganese fraction. It seems likely that the presence of metallic copper catalyzes a faster reduction of the manganese species to metal [94]. The reduction of the Mn100 sample, in the absence of copper, begins at nearly 160 °C and is composed of two peaks with maximums at 315 and 455 °C, which can be attributed to the reduction of  $\text{Mn}^{4+}$  and  $\text{Mn}^{3+}$  cations to  $\text{Mn}^{2+}$ , respectively.



**Figure 3.** H<sub>2</sub>-TPR profiles of Cu-Mn oxide samples.

### 2.1.2. Cobalt-Iron Oxides

The X-ray diffraction patterns of the Co-Fe catalysts in the field of the atomic ratio Fe/(Fe + Co) between 0 and 1 are reported in Figure 4. Data from the textural and phase characterisation of the catalysts are summarized in Table 5. Further data from N<sub>2</sub> sorption are reported in Table S2 and Figure S2. The formation of cubic spinel solid solutions on the whole composition domain can be evidenced, with the only exception of the all-iron sample. The cell parameter of spinel changes with the iron content from 8.09 Å for Co<sub>3</sub>O<sub>4</sub> direct spinel to 8.36 Å for the mostly inverted cobalt ferrite CoFe<sub>2</sub>O<sub>4</sub>. The all-iron sample contains only hematite ( $\alpha$ -Fe<sub>2</sub>O<sub>3</sub>), as expected from the phase diagram in oxidising conditions. The surface area of the mixed spinels, reported in Table 5, is about 80 m<sup>2</sup> g<sup>-1</sup>, nearly twice the surface area of the cobalt and iron oxides end-terms.

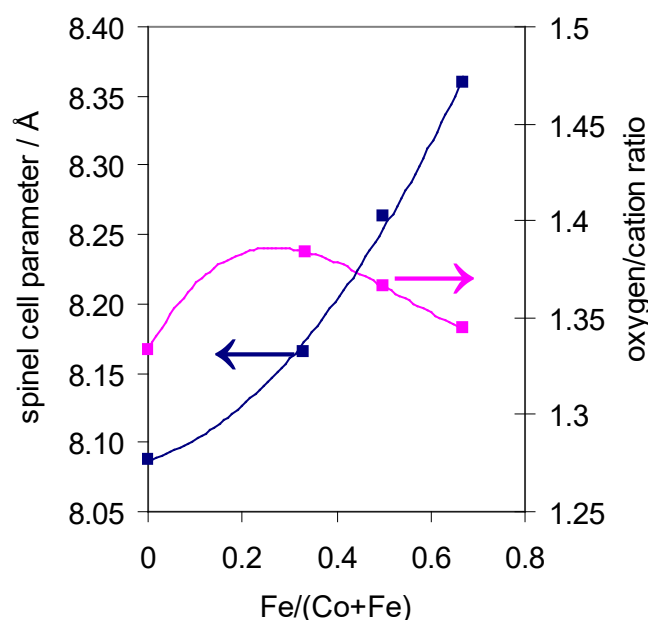


**Figure 4.** Powder XRD patterns of the Co-Fe catalysts. Spinel (◻),  $\alpha$ -hematite (◊).

**Table 5.** Phase and textural characterisation of Co-Fe oxide catalysts.

Catalyst	Phase	Cell Size/Å	S(BET)/m <sup>2</sup> g <sup>-1</sup>	Grain Size/nm	
				Spinel	Hematite
Co100	spinel	8.086 (3)	35	29	
Co67Fe33	spinel	8.167 (4)	81	7	
Co50Fe50	spinel	8.263 (4)	78	11	
Co33Fe67	spinel	8.360 (1)	84	11	
Fe100	$\alpha$ -hematite	5.04, 13.76	43		25

The increase of the cell parameter is not linear with the iron fraction, as indicated in Table 5 and highlighted in Figure 5. The cell size of the samples Fe33Co67 and Fe50Co50 is smaller than the value expected for a Vegard's law solid solution between cobalt spinel Co<sub>3</sub>O<sub>4</sub> and cobalt ferrite CoFe<sub>2</sub>O<sub>4</sub>.

**Figure 5.** Cell size and oxygen/cation ratio of the Co-Fe spinels. The lines are a guide for the eyes.

<sup>57</sup>Fe Mössbauer spectra of two mixed oxides are shown in Figure 6, while the corresponding hyperfine parameters are reported in Table 6. The spectrum of the sample Co67Fe33 is a large quadrupole doublet typical of trivalent iron which can be simply fitted using two spectral components, whereas one of the samples of Co50Fe50 consists of a dominant magnetic distribution component with hyperfine parameters in the typical range of spinels [95], accompanied by a trivalent iron quadrupole doublet. In both cases, they correspond to the typical signature of Fe<sup>3+</sup> and no distinctive signals of Fe<sup>2+</sup> or interchange between Fe<sup>2+</sup> and Fe<sup>3+</sup> are detected. Taking into account the absence of Fe<sup>2+</sup>, the anomalous cell parameters of mixed spinels can be accounted for by the cation distributions reported in Table 7, which imply a substoichiometric cation content. Cation vacancies in non-stoichiometric spinels are known to account for smaller than expected unit cells [96]. The amount of cation vacancies, also reported in Table 7, is a non-linear function of the composition and reaches a maximum for the sample Co67Fe33, *viz.* the sample with the higher deviation from Vegard's law.

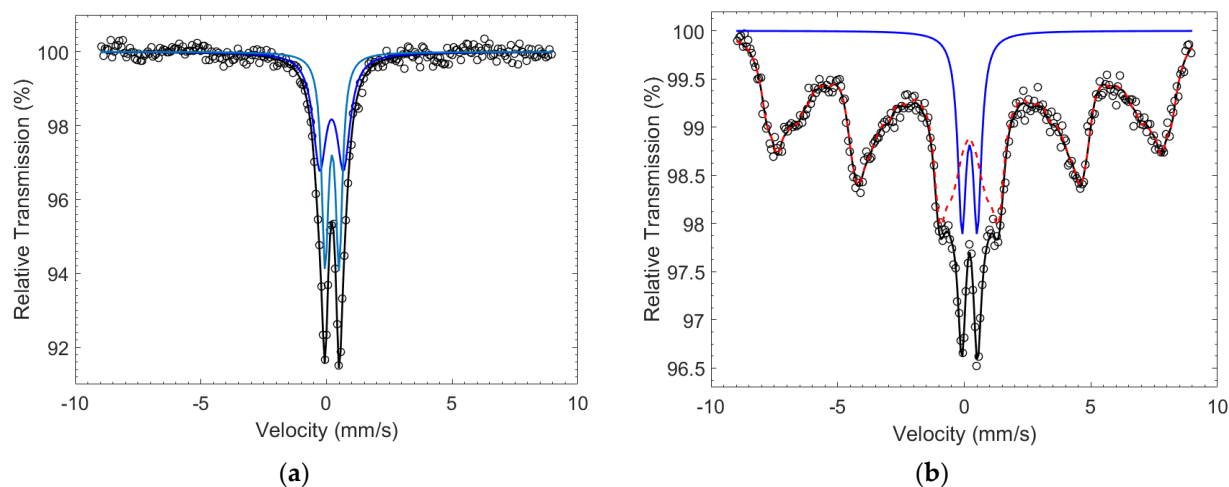


**Figure 6.**  $^{57}\text{Fe}$  Mössbauer spectra of the mixed Co-Fe spinels (a)  $\text{Co}_{67}\text{Fe}_{33}$  and (b)  $\text{Co}_{50}\text{Fe}_{50}$ .

**Table 6.** Room temperature  $^{57}\text{Fe}$  Mössbauer parameters of the Co-Fe oxide catalysts.

Catalyst	$B_{\text{HF}}$ (T)	$\Delta$ (mm/s)	$\delta$ (mm/s)	$\Gamma$ (mm/s)	Area (%)	Site
Co <sub>67</sub> Fe <sub>33</sub>	-	0.95 (8)	0.31 (1)	0.65 (3)	51 (9)	Fe <sup>3+</sup>
	-	0.53 (2)	0.33 (1)	0.32 (3)	49 (9)	Fe <sup>3+</sup>
Co <sub>50</sub> Fe <sub>50</sub>	52-2	0.00 (1)	0.30 (1)	0.6	88 (1)	Fe <sup>3+</sup>
	-	0.60 (2)	0.32 (1)	0.40 (3)	12 (1)	Fe <sup>3+</sup>

**Table 7.** Cation distribution per 4 oxygen atoms in cobalt-iron spinel phases.

Catalyst	Co <sup>2+</sup> Tetr	Fe <sup>3+</sup> Tetr	Co <sup>2+</sup> Oct	Fe <sup>3+</sup> Oct	Co <sup>3+</sup> Oct	Cation Vacancies
Co <sub>100</sub>	1	0	0	0	2	0
Co <sub>67</sub> Fe <sub>33</sub>	0.50	0.50	0.17	0.46	1.26	0.110
Co <sub>50</sub> Fe <sub>50</sub>	0.35	0.65	0.43	0.81	0.68	0.072
Co <sub>33</sub> Fe <sub>67</sub>	1	0.90	0.82	1.08	0.07	0.026

Cation vacancies imply an increase in the oxygen/cation ratio, reported in Figure 5, and the corresponding increase in the average charge of the cations. The increase of the average cation charge brings about a significant decrease in the cell size because trivalent cations are significantly smaller than divalent cations, as is the case for magnetite  $\text{Fe}_3\text{O}_4$  and maghemite  $\gamma\text{-Fe}_2\text{O}_3$ , sharing the same spinel structure with cell size 8.39 and 8.34, respectively.

The strong preference for divalent  $\text{Co}^{2+}$  over trivalent  $\text{Co}^{3+}$  in the tetrahedral site [97] is an important factor in the variation of the number of vacancies with the  $\text{Fe}/(\text{Fe} + \text{Co})$  ratio. In the case of the direct cobalt spinel sample, the energy expenses of introducing  $\text{Co}^{3+}$  in the tetrahedral site render any increase of the average cation charge difficult as the octahedral site is already completely occupied by  $\text{Co}^{3+}$ . For samples of different compositions, the introduction of iron in the material allows the incorporation of trivalent  $\text{Fe}^{3+}$  in the tetrahedral site. The corresponding increase of the inversion degree and the retention of  $\text{Co}^{3+}$  in the octahedral site make possible the increase of the average charge of cations and the corresponding formation of cation vacancies, as observed in the sample  $\text{Co}_{67}\text{Fe}_{33}$ . Further increases in the amount of iron correspond to a decrease of the  $\text{Co}^{3+}$  content and a corresponding decrease in average cation charge and amount of cation vacancies.

The TPR profiles of the Co-Fe catalysts are reported in Figure 7. The consumption of  $\text{H}_2$  in the tests is reported in Table S3. The Co<sub>100</sub> sample presents a first reduction peak with onset at 225 °C and maximum at 325 °C. This first reduction corresponds to 22% of

the hydrogen demand for total reduction and corresponds to the reduction of the cobalt spinel to CoO. The reduction of CoO to cobalt metal is completed in a second peak with a maximum of 425 °C.

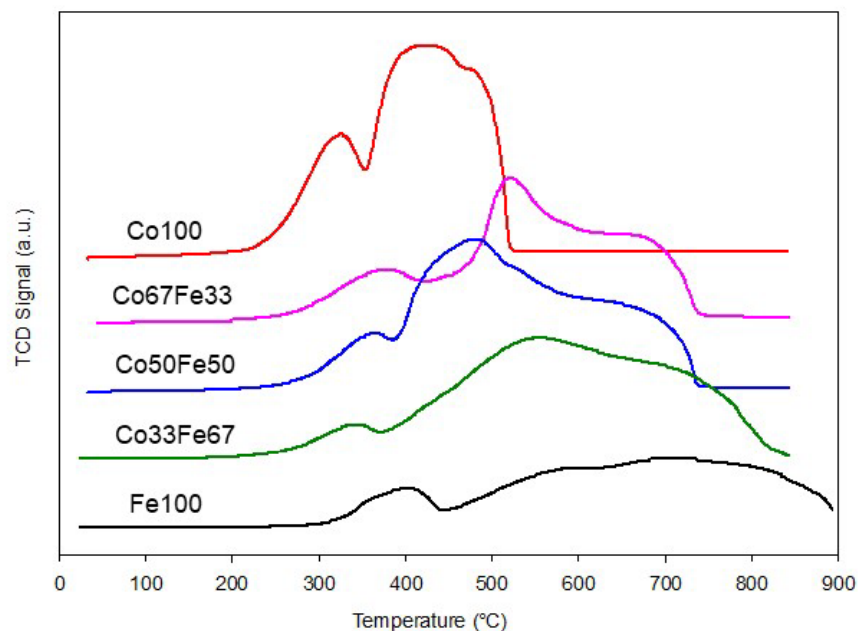


**Figure 7.** H<sub>2</sub>-TPR profiles of Co-Fe oxides.

The three mixed spinel samples present an initial reduction step with an onset at about 260 °C, corresponding to the reduction of Co<sup>3+</sup> to Co<sup>2+</sup>. It is interesting to observe that the delayed onset of reduction of the mixed spinels is similar to what was observed for maghemite-like phases [98]. The temperature of the maximum of this first peak decreases and the corresponding fraction of consumed H<sub>2</sub> decreases from 14 to 5% with the decrease of the amount of cobalt in the sample. The reduction of Co<sup>3+</sup> and the exsolution of CoO destabilize the charge balance of the mixed spinel phase, which decomposes to CoO and an iron spinel phase [94]. The reduction of CoO to metallic Co and that of the iron spinel to FeO are superposed in a complex way and contribute to a signal with a maximum between 480 and 560 °C. The reduction of FeO is completed between 740 and 840 °C.

The reduction of the Fe100 oxide follows the literature pattern [99]. The first peak with an onset at 300° and a maximum at 400 °C consumes 13% of the total hydrogen and corresponds to the reduction of Fe<sub>2</sub>O<sub>3</sub> to Fe<sub>3</sub>O<sub>4</sub>. A second broad peak with a maximum of 590 °C corresponds to the reduction of Fe<sub>3</sub>O<sub>4</sub> to FeO and is partially superposed with the subsequent reduction of FeO to metallic iron. The reduction of the sample is not completed at the final temperature of 900 °C.

## 2.2. HMF Oxidation

### 2.2.1. Blank Tests in the Absence of Catalyst

HMF is very slowly oxidized in aerobic conditions, a degradation rate of about 1% per hour having been observed in aqueous solution at 100 °C under 4 MPa air in the absence of a catalyst [25]. A higher reactivity is observed in the presence of hydroperoxides: HMF in a tert-butyl alcohol solution was converted at 45% by TBHP (molar ratio TBHP/HMF 60) in 12 h at 80 °C, with the formation of DFF, FFCA, DFCA with selectivity, respectively, 23, 60, and 15% [81]. The reactivity was highly solvent-dependent: HMF conversion in DMSO (DMSO/HMF 70) was 8.5% in 12 h at 80 °C, with a selectivity of 15% in DFF and 5% in FDCA.

In our experiments without a catalyst, HMF in the  $\text{CH}_3\text{CN}$  solution was converted at 61% in 3 h at 60 °C at TBHP/HMF ratio 14. In Figure 8, the conversion of HMF and the selectivity of products are reported at 1 and 3 h reaction times. The conversion increased with reaction time from 39 to 61%. The main products were DFF and HMFCFA, the latter with a selectivity slightly higher than the former, 44 and 36%, respectively. The selectivity of both primary oxidation products decreased with the increase of conversion. At the same time, the selectivity of FFCA increased from 9 to 14%, and the selectivity of MA from 2.5 to 5%. The carbon balance correspondingly decreased from 98 to 91%.

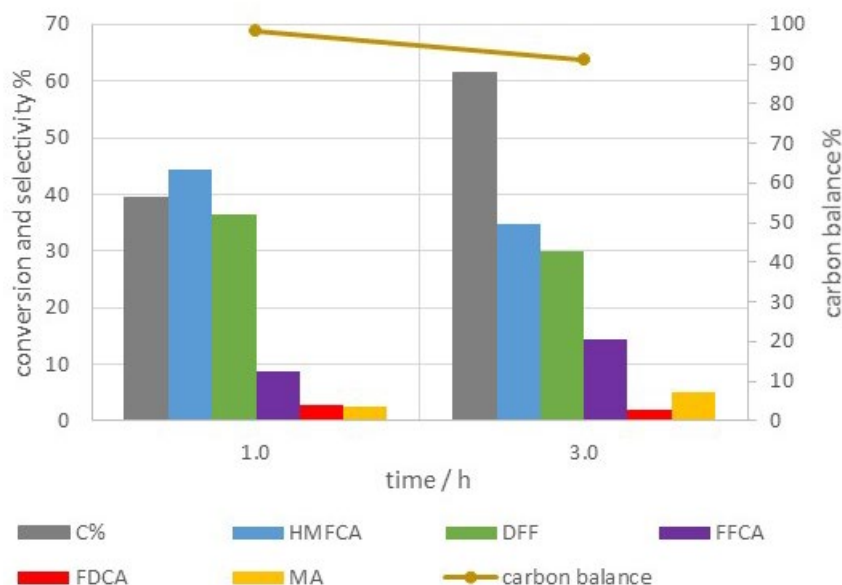


**Figure 8.** Conversion of HMF and selectivity of products in the absence of a catalyst as a function of reaction time. HMF 0.55 M in  $\text{CH}_3\text{CN}$ , TBHP/HMF 14, 60 °C.

The dependence of HMF conversion by the amount of oxidant in the absence of a catalyst has been investigated at 40 °C (Figure 9). The conversion steadily increases with the TBHP/HMF ratio, suggesting an order of reaction from TBHP near 1. At the lowest oxidant amount, DFF and HMFCFA present a nearly identical 44% selectivity. FFCA and FDCA are present with about 2% selectivity. In increasing oxidative conditions, the selectivity of HMFCFA remains virtually constant, whereas the selectivity of DFF decreases, and the selectivity of FFCA and FDCA increases. This behaviour could be attributed to a moderately higher order in the oxidant of the rate of oxidation of DFF (Ox2 in Figure 1) than the rate of oxydehydrogenation of HMFCFA (ODH2 in Figure 1). However, it has to be taken into account that the measured amount of primary intermediates, DFF and HMFCFA, is the result of the sum of the rates of formation and the further conversion of each of them. A lower order in the oxidant of ODH1 than Ox1 reaction in Figure 1 could also justify the observed trend.

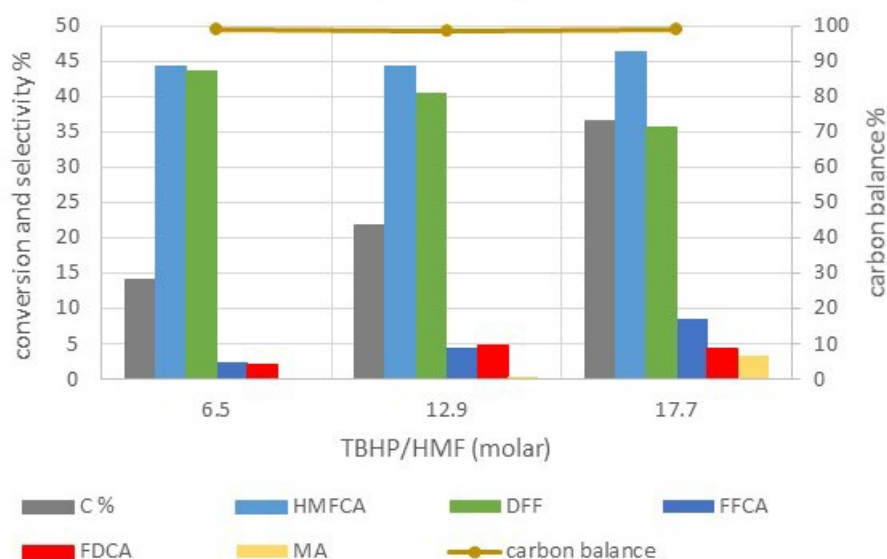


**Figure 9.** Conversion of HMF and selectivity of products in the absence of a catalyst as a function of TBHP/HMF molar ratio. HMF 0.55 M in CH<sub>3</sub>CN, 40 °C, 1 h.

### 2.2.2. Catalytic Tests on Copper-Manganese Oxides

Before comparing the catalytic activity of Cu-Mn catalysts with different compositions, it is useful to follow the temperature dependence of the activity on a typical catalyst, Cu<sub>67</sub>Mn<sub>33</sub>, the acronym of the catalyst indicating the cation percent ratio. At TBHP/HMF ratio 7 and 1 h reaction time, conditions milder than the ones used in most tests, the conversion of HMF rises from 15% at room temperature to 95% at 60 °C and 100% at 80 °C (Figure 10).

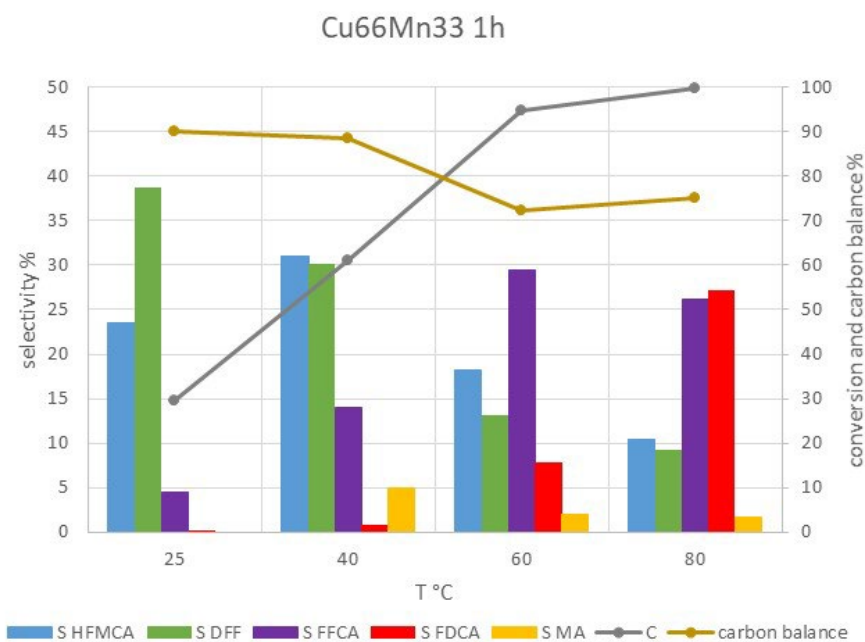


**Figure 10.** Conversion, selectivity, and carbon balance on catalyst Cu<sub>67</sub>Mn<sub>33</sub> as a function of the temperature of the reaction. The lines are a guide for the eye. Reaction conditions: TBHP/HMF 7 (molar ratio), HMF/catalyst 4 (*w/w*), 1 h.

At 25 °C, the selectivity of DFF and HMFCA are, respectively, 38 and 23%, and only 5% for further oxidation products. At increasing temperature, the selectivity of DFF decreases, and the selectivity of HMFCA increases, in parallel with the increase of FFCA selectivity to 14%. This trend allows several interpretations, differing by the step of oxidation, which is considered prevalent. On one hand, the higher activation energy of the formation of FFCA by Ox2 reaction of DFF than by ODH2 reaction of HMFCA could justify the data. On the other hand, the higher activation energy of the Ox1 formation of HMFCA than ODH1 formation of DFF could also account for the observed trend. Indeed, the higher activation energy for the oxidation of aldehyde than for the oxidation of alcohol was classically observed in the gas phase [100].

The selectivity of FFCA increases with temperature from 5% at 25 °C to 30% at 60 °C. It starts to decrease when it is overcome by its conversion to FDCA, whose selectivity increases from 1% at 40 °C to 27% at 80 °C. The sequential nature of the reactions depicted in Figure 1 is clearly shown by the comparison of the results at an increasing temperature in Figure 10. It also appears that the activation energies of the Ox1 and ODH1 reactions of HMF oxidation are lower than the activation energies of FFCA formation, which is itself lower than the activation energy of the Ox3 oxidation of FFCA to FDCA.

The carbon balance is 90% for reaction temperatures up to 40 °C and worsens to 72–75% at 60 or 80 °C. Humins, oligomers, or products deriving from condensation/transformation of the reaction intermediates are critical by-products in most processes involving HMF. Some of these by-products form by a complex mechanism involving the hydration of the carbon in  $\alpha$  to the enol group of HMF, followed by the opening of the furanic ring with the formation of 2,5-dioxo-6-hydroxy-hexanal (DHH) and keto-enol condensation [101,102]. It has been suggested that the propagation of the oligomers can occur by condensation of the enol groups of DHH or of the oligomers themselves with any ketone or aldehyde present in the system. However, the unclear question is whether these by-products form only from HMF, or from also the reaction intermediates and whether the generation of radical-type oxygen species promotes their formation. Indeed, in our experiments, oligomers are more and more formed from the onset of the reaction up to a high degree of advancement of the oxidation, when the concentration of HMF is no more significant. This suggests that they are formed by condensation not just of HMF, but also of all carbonyl-bearing molecules involved in the process, namely HMF, DFF, and FFCA.

The dependence of the activity on the composition of the catalyst in the Cu-Mn series is shown in Figure 11 for 3 h conversion of HMF at 60 °C with TBHP/HMF ratio 13. In these conditions, all the copper-bearing catalysts present a conversion near 100%. The Cu100 catalyst, with only the CuO phase, is highly active despite its low surface area of 11 m<sup>2</sup> g<sup>-1</sup>, the lowest among our catalysts. The oxidation ratios (FFCA + FDCA)/(HMFCA + DFF) and FDCA/FFCA, reported in Table 8, are two useful tools for a first-glance evaluation of the oxidation activity. In the reaction scheme of Figure 1, the two ratios are related to the degree of advancement of, respectively, the conversion of the primary oxidation products to FFCA and the conversion of FFCA to FDCA. Among the Cu-bearing catalysts, the two ratios evolve with the composition of the catalyst in a parallel way, the lowest for Cu100 and the highest for Cu67Mn33. The oxidation ratios of Cu50Mn50 and Cu33Mn67 progressively decrease with the decrease of the copper content (Table 8), accompanied by a decrease in the specific surface area of the samples, from 106 m<sup>2</sup> g<sup>-1</sup> for Cu67Mn33 to 51 m<sup>2</sup> g<sup>-1</sup> for Cu33Mn67 (Table 4).

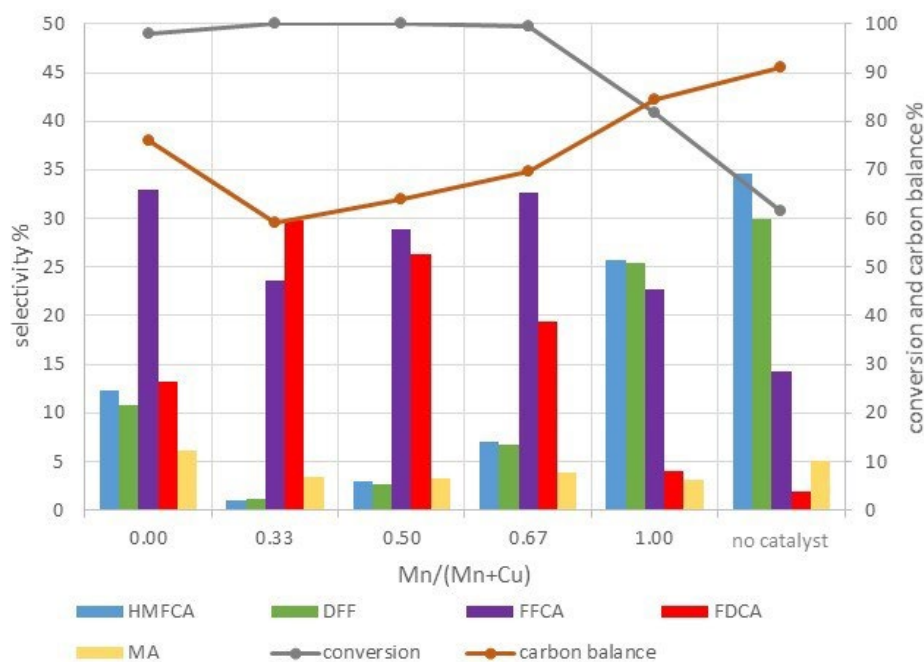


**Figure 11.** Conversion, selectivity, and carbon balance on Cu-Mn oxide catalysts and in the absence of a catalyst. The lines are a guide for the eye. Reaction conditions: TBHP/HMF 13 (molar ratio), HMF/catalyst 4 (*w/w*), 60 °C, 3 h.

**Table 8.** Product ratios and HMF reaction rates on different catalysts.

Catalyst	(FFCA + FDCA)/ (HMFCFA + DFF)	FDCA/FFCA	HMF Reaction Rate (mmol g <sup>-1</sup> h <sup>-1</sup> )
Cu100	2.00	0.40	10.1
Cu67Mn33	23.30	1.26	10.2
Cu50Mn50	10.05	0.91	11.4
Cu33Mn67	3.78	0.60	11.2
Mn100	0.52	0.18	8.9
Co100	0.87	0.26	9.4
Co67Fe33	8.70	0.79	11.2
Co50Fe50	1.73	0.43	10.3
Co33Fe67	0.53	0.20	9.6
Fe100	0.25	0.18	5.5
no catalyst	0.26	0.12	-

Reaction conditions: TBHP/HMF 13 (molar ratio), HMF/catalyst 4 (*w/w*), 60 °C, 3 h.

The definition of a correlation between the composition of the catalyst and the activity is complicated by the polyphasic nature of the samples. In the case of the only monophasic catalyst, CuO, high activity as a Fenton catalyst is not unexpected [103,104]. Significant fractions of CuO with grain sizes much smaller than in Cu100 are present in Cu67Mn33 and Cu50Mn50 samples. However, the pattern of activity of these catalysts is very different from Cu100, with the (FFCA + FDCA)/(HMFCFA + DFF) ratio up to an order of magnitude higher.

The carbon balance is quite poor on all Cu-bearing samples, following a trend inversely proportional to the trend of the oxidation ratios, with the worse value on Cu67Mn33, the most FDCA-producing catalyst. This strongly suggests attributing most of the deficit of carbon balance to the condensation or conversion of highly oxidized products. The Mn100 catalyst presents a lower activity (81%) and lower oxidation ratios than

any Cu-bearing catalyst (Table 8). It is indeed known that manganese oxides are quite effective Fenton catalysts but they can also lead to a decrease in the availability of the oxidant by unselective degradation of the hydroperoxide [105–107].

It can also be observed that, at 60 °C and a high oxidant ratio, HMFCFA and DFF were measured in similar amounts on all our catalysts, despite minor variations. This behaviour, which suggests a similar rate between reactions of aldehyde oxidation and alcohol oxydehydrogenation, is relatively uncommon in HMF oxidation catalysis and has already been observed only on mixed oxide catalysts [73,76,81]. The observation of relatively similar amounts of HMFCFA and DFF also in the blank tests could suggest an important radical contribution to the first steps of oxidation, unhindered by the presence of the catalyst. It has been observed that the adsorption of organic acids has an inhibiting effect on the activity of heterogeneous Fenton catalysts [108]. This could justify the poor oxidation ratios in the blank and on the CuO and manganese oxides, the Fenton catalysts are expected to be the best. Conversely, this could suggest a direct implication of the oxygen of the catalyst in the mixed oxides, the most effective FDCA producers.

### 2.2.3. Catalytic Tests on Cobalt-Iron Oxides

The dependence of the activity on the composition of the catalyst in the Co-Fe series is shown in Figure 12. The change of the activity with the composition of the catalyst follows a volcano-type trend, with a low activity of the single-cation end-term oxides and higher activity of the intermediate mixed oxides, featuring a maximum for an iron fraction of 0.33. The carbon balance follows a trend opposite to the conversion, confirming the implication of oxidation products in the formation of converted species. The comparison of the activities of the three mixed Co-Fe spinels suggests some peculiarities of the Co-Fe system. Indeed, the three solid solution materials present nearly identical surface areas (see Table 5), but very different activities. A sharp decrease in conversion, with a corresponding improvement of the carbon balance, is observed for Fe fractions higher than 0.33, interestingly following the same trend of variation in the number of cation vacancies (see Figure 5).

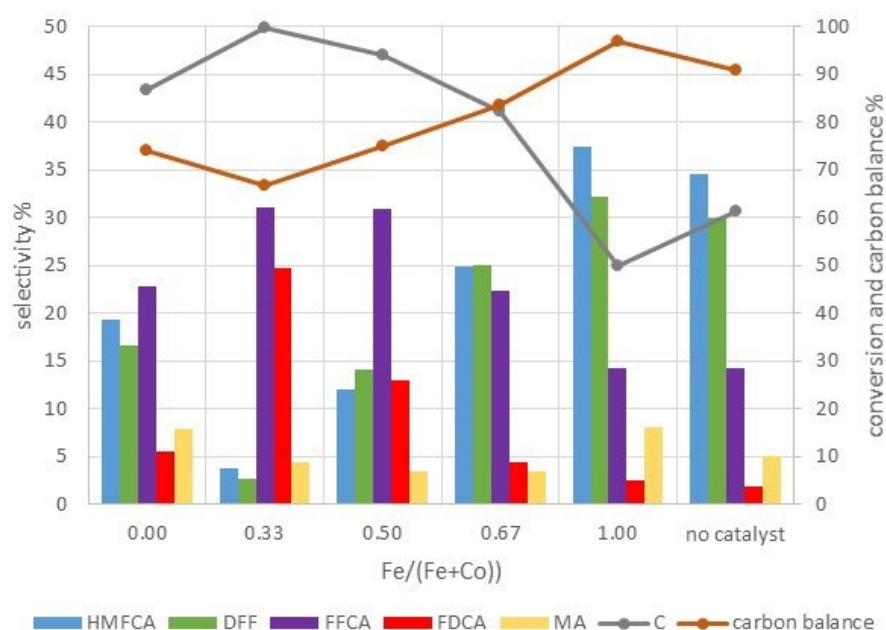


**Figure 12.** Conversion, selectivity, and carbon balance on Fe-Co oxide catalysts and in the absence of a catalyst. The lines are a guide to the eye. Reaction conditions: TBHP/HMF 13 (molar ratio), HMF/catalyst 4 (*w/w*), 60 °C, 3 h.

Fe100, the Fe end-member of the series of catalysts with  $\alpha$ -hematite structure, presents the same product distribution as the blank test, with a 10% lower conversion. Hematite has been used as a cheap Fenton catalyst [109], and its anti-catalytic behaviour could be attributed to unselective hydroperoxide degradation.

### 3. Discussion

The importance of blank tests in the evaluation of HMF oxidation by TBHP has to be stressed. In the absence of catalysts, HMF conversion as high as 60% has been observed (Figure 8). The products formed were essentially HMFCa and DFF, while few FFCA and virtually no FDCA were observed. This suggests that HMF is a more effective substrate for alcohol oxidation or aldehyde oxydehydrogenation than, respectively, HMFCa or DFF (see Figure 1). Another possible interpretation is that the formation of acid groups by the initial oxydehydrogenation reaction decreases the pH of the solution and stabilizes TBHP in the absence of a catalyst.

The presence of oxide catalysts affected the oxidation reactions in a way highly dependent on the nature of the oxide. In the case of the Fe100 catalyst ( $\alpha$ -hematite), the most acidic of our catalysts [110], conversion and selectivity were comparable to the blank test results (Figure 12). For other single-cation oxides, like Co100 and Mn100, the activity was slightly higher than the blank, a result already observed in aerobic oxidation of HMF on Co and Mn oxides [111].

It has to be remarked that the patterns of variation of the catalytic activity with the composition of the mixed oxides are very similar in the two different systems, Cu-Mn and Fe-Co. The Co-Fe catalysts present a lower activity compared to the Cu-Mn ones but the two systems present a maximum of oxidation activity for a 0.33 fraction of the more charged cation, with a decrease of activity when this fraction increases. In the case of the Cu-Mn system, this pattern could be tentatively justified by a different surface area and tenorite content in the samples. In the case of the Co-Fe system, however, the samples from Co33Fe67 to Co67Fe33 are monophasic spinels and present the same surface area. In this case, no other factors beyond the pattern of cation vacancies seem to affect the trend of oxidation activity. Quite interestingly, the literature on the site occupancy in the Cu-Mn spinels suggests a pattern of cation vacancies similar to the one observed in the Co-Fe spinels [90].

The increase of oxidation activity with the number of cation defects is not suggestive of a radical mechanism, as more cation defects in a spinel structure correspond to a higher oxidation state of the cations. In these conditions, it seems unlikely that the reaction rates, at least for the oxidation of DFF and HMFCa, depend on a surface radical mechanism. It has been shown that maghemite  $\gamma$ -Fe<sub>2</sub>O<sub>3</sub>, with only Fe<sup>3+</sup> cation, is less active in radical promotion than magnetite  $\alpha$ -Fe<sub>2</sub>O<sub>3</sub>, with both Fe<sup>2+</sup> and Fe<sup>3+</sup> cations [112–114].

The implication of lattice oxygen in the mechanism is a tempting alternative hypothesis. Admittedly, the onset of catalyst reduction, as derived from TPR experiments (see Figures 3 and 7), is virtually constant with the composition of the mixed spinels, either in the Cu-Mn or Co-Fe systems. It is evident that no simple specific relation could be observed between catalyst redox properties and the catalytic behaviour. Indeed, the role of cation vacancies in oxidation catalysts has been evocated several times but never solidly established. Cation defects have been related to the formation of peroxo and superoxo species at the surface of spinels and have been suggested to favour the implication of lattice oxygen in oxidation reactions at relatively high temperatures [115,116]. Cation vacancies in mixed scheelite have been suggested to favour the extraction of olefin  $\alpha$ -hydrogens, but this effect has been seriously questioned [117]. Interestingly, cation vacancies in FeV spinel catalysts for methanol oxidation have been shown to increase the selectivity of formaldehyde by increasing the basicity of the catalyst [118]. The possible role of spinel cation vacancies in the oxidation of HMF seems clearly worthy of further investigation. Indeed, a mixed spinel usually presents both higher basicity and higher acidity than their single-oxide end-terms [119,120].

HMF oxidation rate in our tests was systematically higher than in experiments on other unsupported oxide catalysts (see Tables 3 and 8). In the cases in the literature, high conversion was reached at a higher temperature than in our reaction conditions [73,75,76,81,121], suggesting that a relatively low reaction temperature represents an optimum between oxygen development from TBHP and catalytic activity. However, the carbon balance of our tests at high conversion was definitely poor (Figures 11 and 12). The carbon balance presented an inverse correlation with the conversion and selectivity of FDCA. It is likely that most loss of carbon has to be attributed to consecutive reactions of condensation or overoxidation of the analysed oxidation products [122–124]. Reports in the literature indicate that most condensation products from HMF oxidation can be removed from mixed oxide catalysts by solvent washing, providing satisfactory recyclability of the catalysts [73,75,81,125].

The observed unfavourable selectivity-conversion correlation suggests that better results could be obtained by a moderation of the reaction conditions. Dong observed a significant decrease in the formation of coproducts with a decrease in the surface area and the oxygen adsorption of the biphasic  $(\text{Cu}, \text{Mn})_3\text{O}_4$  and  $\text{MnO}_2$  catalyst [125]. In our system, a possible pathway to improve selectivity could be a change of oxidant from TBHP to molecular  $\text{O}_2$ . TBHP has been systematically shown to increase the reaction rate of oxidation by comparison with the use of dissolved oxygen [73,75,81]. An expected decrease of conversion with a shift to aerobic oxidation could be compensated by the introduction of a dissolved hydroxide [83,84], despite that it could be difficult to foresee in which way an added base could influence the properties of the surface sites of the catalyst [126].

## 4. Materials and Methods

### 4.1. Synthesis of Catalysts

Two series of mixed oxide catalysts with nominal composition  $\text{M}^{\text{A}}_{3-x}\text{M}^{\text{B}}_x\text{O}_4$  have been prepared, with  $\text{M}^{\text{A}} = \text{Co}$  and  $\text{M}^{\text{B}} = \text{Fe}$  or  $\text{M}^{\text{A}} = \text{Cu}$  and  $\text{M}^{\text{B}} = \text{Mn}$ . In each series, cation fractions  $\text{M}^{\text{B}}/(\text{M}^{\text{A}} + \text{M}^{\text{B}})$  were targeted as 0.00, 0.33, 0.50, 0.67, and 1.00. The catalysts were named from their cation percent ratio, for instance, Cu67Mn33. The reagents used were  $\text{Fe}(\text{NO}_3)_3 \cdot 9\text{H}_2\text{O}$ ,  $\text{CoCl}_2$ ,  $\text{CuCl}_2 \cdot \text{H}_2\text{O}$ ,  $\text{Mn}(\text{NO}_3)_2 \cdot 4\text{H}_2\text{O}$ , and NaOH from Sigma-Aldrich (Saint Louis, MI, USA).

Nanoparticulate oxide catalysts were prepared by coprecipitation in an alkaline solution [127,128]. In total, 0.5 M aqueous solutions of  $\text{M}^{\text{I}}$  salt and 1 M aqueous solutions of  $\text{M}^{\text{II}}$  salt in the stoichiometric desired ratio were mixed and added dropwise into 0.8 M aqueous solution of NaOH at room temperature in 2 h of stirring with a pH kept at 12. The precipitate was isolated by vacuum filtration and washed with demineralized water to remove  $\text{Na}^+$  and anions, then dried overnight in the air at 120 °C and calcined in flowing air at 450 °C for 6 h.

### 4.2. Characterisation Methods

The solids were characterised by X-ray powder diffraction (Bragg-Brentano  $\theta$ - $\theta$  Bruker D8 Advance diffractometer, Bruker Lynx Eye detector, Cu  $\text{K}\alpha$  radiation), energy-dispersive X-ray analysis (Quanta 200F SEM EDS FEI, 15 kV accelerating voltage),  $\text{H}_2$  temperature programmed reduction (TPR, Micromeritics AutoChem-II 2920 equipped with a TCD detector), and  $\text{N}_2$  physisorption (Micromeritics Tristar apparatus with improved vacuum system, samples preactivated at 250 °C under vacuum).

$^{57}\text{Fe}$  Mössbauer spectra were measured with a  $^{57}\text{Co}$  source embedded in a rhodium matrix. The measurements were performed keeping the source at room temperature while the absorber temperature has been varied between 5 and 300 K using a helium-flow cryostat. The spectrometer was operated with a triangular velocity waveform, and a gas-filled proportional counter was used for the detection of the gamma rays. Velocity calibration was performed with an  $\alpha$ -Fe foil. The spectra were fitted with an appropriate combination of Lorentzian lines. In this way, spectral parameters such as the isomer shift ( $\delta$ ),

the electric quadrupole splitting ( $\Delta$ ), the linewidth at half maximum ( $\Gamma$ ), the hyperfine fields ( $B_{\text{HF}}$ ), and the relative absorption areas (Area) of the different components were determined.

For all samples, the elemental analysis indicated a composition within 1% of the expected cation ratio. The surface area of the samples was evaluated by the BET method, grain size from Williamson–Hall plots for monophasic samples, and the Scherrer method for multiphasic samples.

The cation distribution in the spinel phases was evaluated by best-fitting the cell parameter by the formula  $a = (8/(11.3^{0.5}))(5d_{\text{A-O}} + (33d_{\text{B-O}}^2 - 8d_{\text{A-O}}^2)^{0.5})$  [93,129,130]. The A–O bond lengths of the tetrahedral site were assumed as 1.865 and 1.975 Å, respectively, for  $\text{Fe}^{3+}$  and  $\text{Co}^{2+}$ . The B–O bond lengths of the octahedral site were assumed as 1.9, 2.025, 2.1, and 2.12 Å, respectively, for  $\text{Co}^{3+}$ ,  $\text{Fe}^{3+}$ ,  $\text{Co}^{2+}$ , and  $\text{Fe}^{2+}$  [93,131]. The parameters of Lavina et al. [86] have been used for the influence of cation vacancies on cell size. Redox properties were evaluated by  $\text{H}_2$ -TPR, for which 50 mg of catalyst in 200 mg of SiC was pretreated with He at 150 °C for 90 min prior to the analysis in 5%  $\text{H}_2$  in Ar from room temperature to 850 °C with a ramp of 20 °C/min.

The surface area was evaluated by the BET method. Pore size distribution was determined by a DFT kernel [132]. Pore volume was measured by the  $\alpha\text{S}$  method when a defined adsorption plateau was present. In other rare cases, the pore volume was assumed as the adsorbed amount at  $p/p^\circ$  0.975, corresponding to the adsorbed amount in pores with a diameter of 50 nm.

#### 4.3. Catalytic Tests

The reagents and standards used were HMF, tert-butyl hydroperoxide (t-BuOOH, 5.5 M in decane), acetonitrile (MeCN), decane, methanol (MeOH), maleic anhydride (MA), FDCA, 2,5-diformylfuran (DFF) from Sigma-Aldrich (Saint Louis, Missouri, USA), 5-hydroxymethyl-2-furancarboxylic acid (HMFCFA) from abcr (Karlsruhe, Germany), and 5-formyl-2-furancarboxylic acid (FFCA) from TCI Chemicals (Tokyo, Japan), respectively.

The oxidation of HMF was carried out in a Parr 5000 Multiple Reactor System (Parr Instrument Company, Moline, Illinois, USA) equipped with 6 autoclave reactors (75 cm<sup>3</sup> stainless steel T316), each with a mechanical stirrer and measurement tools for temperature and pressure. In a typical activity test, 126 mg of HMF (1 mmol) was dissolved in 2 mL of MeCN. Subsequently, a catalyst (30 mg, about 0.1 mmol of  $\text{M}^{3-x}\text{M}^{\text{II}}\text{O}_4$ ) and 1.3 or 2.6 mL of t-BuOOH solution (respectively 7 or 14 mmol) were added to the reactor. Reactions were conducted for 1 to 3 h at a temperature from 20 to 60 °C under constant magnetic stirring (450 rpm). Blank tests were carried out in the same conditions in the absence of a catalyst. At the end of the reaction, 1.7 mL of MeOH was injected in order to dissolve the precipitated FDCA [133]. The catalyst was separated by centrifugation and the recovered solutions were analysed by HPLC on a Shimadzu (Kyoto, Japan) LC-20AD apparatus equipped with Bio-Rad (Hercules, CA, USA) 125-0131 Cartridge Holder (30 mm × 4.6 mm) and Bio-Rad Aminex HPX-87H (300 mm × 7.8 mm) pre-packed column and UV detector at 254 nm. A 0.005 M  $\text{H}_2\text{SO}_4$  mobile phase was employed as eluent at 30 °C with a flow rate of 0.6 mL/min for 60 min.

The average standard error between duplicated activity tests was lower than 1%. The species analysed were HMF, DFF, HMFCFA, FFCA, FDCA, and MA. Part of maleic anhydride formed methylated species during the recovery of the products by methanol washing. This amount was taken into account in the evaluation of maleic anhydride. The conversion was measured from measured concentrations as  $(C_{\text{HMF}}^{\text{initial}} - C_{\text{HMF}}^{\text{final}})/C_{\text{HMF}}^{\text{initial}}$  and selectivity as  $C_{\text{product}}^{\text{final}}/(C_{\text{HMF}}^{\text{final}} - C_{\text{HMF}}^{\text{initial}})$ . The carbon balance was evaluated as the difference between the conversion of HMF and the sum of analysed products.

## 5. Conclusions

Noble metal-free catalysts based on earth-abundant and inexpensive mixed oxides are active catalysts of all steps of the reaction cascade leading from HMF to FDCA using TBHP as an oxidation agent. The nature and composition of the catalyst significantly affect the reactivity and the distribution of the products. In most cases, the analysis of the results provides evidence that radical-type oxygen species, deriving from the t-BuOOH activation, play a determining role in the performances. The role of the catalysts is thus mainly to promote the activation of t-BuOOH and the generation of active oxidizing species. However, beyond the initial steps of HMF oxidation, the trend of reactivity with the degree of oxidation of the material does not correspond to the expected behaviour of a heterogeneous Fenton mechanism, and some implications of the lattice oxygen in the reaction mechanism can be postulated.

The similar rate of oxidation of the alcohol and aldehyde groups of HMF, both in the presence and the absence of the catalyst, indicates that the oxides do not significantly affect the selectivity of the early steps of HMF oxidation. The examined mixed oxides do not appear as effective catalysts for the selective formation of DFF. Degradation and condensation of the oxidation products remain an important issue, which is to be mainly dealt with by the choice of process conditions. The increase of the activation energy of oxidation with the advancement of the reaction cascade suggests temperature as a valuable tool to control the relative selectivity of the formation of FFCA and FDCA.

**Supplementary Materials:** The following supporting information can be downloaded at: [www.mdpi.com/article/10.3390/catal12080814/s1](http://www.mdpi.com/article/10.3390/catal12080814/s1), Figure S1: N<sub>2</sub> sorption isotherms at 77 K and pore size distribution for samples of the Cu-Mn series; Figure S2: N<sub>2</sub> sorption isotherms at 77 K and pore size distribution for samples of the Co-Fe series; Table S1: Phase composition of Cu-Mn oxide catalysts; Table S2: Textural data from N<sub>2</sub> sorption experiments; Table S3: Uptake of H<sub>2</sub> in TPR tests.

**Author Contributions:** Conceptualization, F.Q., G.C. and F.D.R.; methodology, O.G. and R.A.; validation, R.A., N.T. and S.P.; formal analysis, L.S. and F.D.R.; investigation, A.E.D. and M.T.S.; resources, N.T.; writing—original draft preparation, A.E.D. and G.C.; writing—review and editing, L.S. and F.D.R.; supervision, S.P. and F.D.R. All authors have read and agreed to the published version of the manuscript.

**Funding:** This research was funded by the Erasmus Mundus Action 1 Programme Joint Doctorate SINCHEM (Sustainable INDUSTRIAL CHEMistry) (FPA 2013-0037) and by the COST Action CA18220 European network Fur4Sustain (FURan based chemicals and materials FOR a SUSTAINable development).

**Institutional Review Board Statement:** Not applicable.

**Informed Consent Statement:** Not applicable.

**Data Availability Statement:** Data are provided within the article and in Supplementary Materials.

**Acknowledgments:** Thanks are due to Thomas Cacciaguerra and Géraldine Layrac for technical support in the characterisation of the catalysts.

**Conflicts of Interest:** The authors declare no conflict of interest.

## References

1. Bozell, J.J.; Petersen, G.R. Technology development for the production of biobased products from biorefinery carbohydrates—the US Department of Energy’s “Top 10” revisited. *Green Chem.* **2010**, *12*, 539–554.
2. Eerhart, A.J.J.E.; Faaij, A.P.C.; Patel, M.K. Replacing fossil based PET with biobased PEF; process analysis, energy and GHG balance. *Energy Environ. Sci.* **2012**, *5*, 6407–6422.
3. Service, R.F. Sugary Recipe Boosts Grow-Your-Own Plastics. *Science* **2006**, *312*, 1861.
4. Roman-Leshkov, Y.; Barrett, C.J.; Liu, Z.Y.; Dumesic, J.A. Production of dimethylfuran for liquid fuels from biomass-derived carbohydrates. *Nature* **2007**, *447*, 982–986.
5. Van Putten, R.J.; van der Waal, J.C.; de Jong, E.; Rasdendra, C.B.; Heeres, H.J.; de Vries, J.G. Hydroxymethylfurfural, A Versatile Platform Chemical Made from Renewable Resources. *Chem. Rev.* **2013**, *113*, 1499–1597.

6. Gandini, A.; Lacerda, T.M.; Carvalho, A.J.F.; Trovatti, E. Progress of Polymers from Renewable Resources: Furans, Vegetable Oils, and Polysaccharides. *Chem. Rev.* **2016**, *116*, 1637–1669.
7. Zhu, Y.; Romain, C.; Williams, C.K. Sustainable polymers from renewable resources. *Nature* **2016**, *540*, 354–362.
8. Huang, Y.T.; Wong, J.J.; Huang, C.J.; Li, C.L.; Jang, G.W.B. 2,5-Furandicarboxylic Acid Synthesis and Use. In *Chemicals and Fuels from Bio-Based Building Blocks*; Cavani, F., Albonetti, S., Basile, F., Gandini, A., Eds.; Wiley-VCH: Weinheim, Germany, 2016; pp. 191–215.
9. Du, Z.; Ma, J.; Wang, F.; Liu, J.; Xu, J. Oxidation of 5-hydroxymethylfurfural to maleic anhydride with molecular oxygen. *Green Chem.* **2011**, *13*, 554–557.
10. Patil, S.K.R.; Lund, C.R.F. Formation and Growth of Humins via Aldol Addition and Condensation during Acid-Catalyzed Conversion of 5-Hydroxymethylfurfural. *Energy Fuels* **2011**, *25*, 4745–4755.
11. Tsilomelekis, G.; Orella, M.J.; Lin, Z.; Cheng, Z.; Zheng, W.; Nikolakis, V.; Vlachos, D.G. Molecular structure, morphology and growth mechanisms and rates of 5-hydroxymethyl furfural (HMF) derived humins. *Green Chem.* **2016**, *18*, 1983–1993.
12. Casanova, O.; Iborra, S.; Corma, A. Biomass into Chemicals: Aerobic Oxidation of 5-Hydroxymethyl-2-furfural into 2,5-Furandicarboxylic Acid with Gold Nanoparticle Catalysts. *ChemSusChem* **2009**, *2*, 1138–1144.
13. Wan, X.; Zhou, C.; Chen, J.; Deng, W.; Zhang, Q.; Yang, Y.; Wang, Y. Base-Free Aerobic Oxidation of 5-Hydroxymethyl-furfural to 2,5-Furandicarboxylic Acid in Water Catalyzed by Functionalized Carbon Nanotube-Supported Au–Pd Alloy Nanoparticles. *ACS Catal.* **2014**, *4*, 2175–2185.
14. Wojcieszak, R.; Santarelli, F.; Paul, S.; Dumeignil, F.; Cavani, F.; Gonçalves, R.V. Recent Developments in maleic acid synthesis from bio-based chemicals. *Sustain. Chem. Process.* **2015**, *3*, 9.
15. Li, S.; Su, K.; Li, Z.; Cheng, B. Selective oxidation of 5-hydroxymethylfurfural with H<sub>2</sub>O<sub>2</sub> catalyzed by a molybdenum complex. *Green Chem.* **2016**, *18*, 2122–2128.
16. Davis, S.E.; Houk, L.R.; Tamargo, E.R.; Datye, A.K.; Davis, R.J. Oxidation of 5-hydroxymethylfurfural over supported Pt, Pd and Au catalysts. *Catal. Today* **2011**, *160*, 55–60.
17. Xu, C.; Paone, E.; Rodriguez-Padron, D.; Luque, R.; Mauriello, F. Recent catalytic routes for the preparation and the upgrading of biomass derived furfural and 5-hydroxymethylfurfural. *Chem. Soc. Rev.* **2020**, *49*, 4273–4306.
18. Zhang, Z.; Deng, K. Recent Advances in the Catalytic Synthesis of 2,5-Furandicarboxylic Acid and Its Derivatives. *ACS Catal.* **2015**, *5*, 6529–6544.
19. Zhao, D.; Su, T.; Wang, Y.; Varma, R.S.; Len, C. Recent advances in catalytic oxidation of 5-hydroxymethylfurfural. *Mol. Catal.* **2020**, *495*, 111133.
20. Hameed, S.; Lin, L.; Wang, A.; Luo, W. Recent Developments in Metal-Based Catalysts for the Catalytic Aerobic Oxidation of 5-Hydroxymethyl-Furfural to 2,5-Furandicarboxylic Acid. *Catalysts* **2020**, *10*, 120.
21. Han, X.; Li, C.; Guo, Y.; Liu, X.; Zhang, Y.; Wang, Y. N-doped carbon supported Pt catalyst for base-free oxidation of 5-hydroxymethylfurfural to 2,5-furandicarboxylic acid. *Appl. Catal. A Gen.* **2016**, *526*, 1–8.
22. Zhang, Y.; Xue, Z.; Wang, J.; Zhao, X.; Deng, Y.; Zhao, W.; Mu, T. Controlled deposition of Pt nanoparticles on Fe<sub>3</sub>O<sub>4</sub>@carbon microspheres for efficient oxidation of 5-hydroxymethylfurfural. *RSC Adv.* **2016**, *6*, 51229–51237.
23. Han, X.; Geng, L.; Guo, Y.; Jia, R.; Liu, X.; Zhang, Y.; Wang, Y. Base-free aerobic oxidation of 5-hydroxymethylfurfural to 2,5-furandicarboxylic acid over a Pt/C–O–Mg catalyst. *Green Chem.* **2016**, *18*, 1597–1604.
24. Zhou, C.; Deng, W.; Wan, X.; Zhang, Q.; Yang, Y.; Wang, Y. Functionalized Carbon Nanotubes for Biomass Conversion: The Base-Free Aerobic Oxidation of 5-Hydroxymethyl-furfural to 2,5-Furandicarboxylic Acid over Platinum Supported on a Carbon Nanotube Catalyst. *ChemCatChem* **2015**, *7*, 2853–2863.
25. Ait Rass, H.; Essayem, N.; Besson, M. Selective Aerobic Oxidation of 5-HMF into 2,5-Furandicarboxylic Acid with Pt Catalysts Supported on TiO<sub>2</sub>- and ZrO<sub>2</sub>-Based Supports. *ChemSusChem* **2015**, *8*, 1206–1217.
26. Miao, Z.; Wu, T.; Li, J.; Yi, T.; Zhang, Y.; Yang, X. Aerobic oxidation of 5-hydroxymethylfurfural (HMF) effectively catalyzed by a Ce<sub>0.8</sub>Bi<sub>0.2</sub>O<sub>2-δ</sub> supported Pt catalyst at room temperature. *RSC Adv.* **2015**, *5*, 19823–19829.
27. Siankevich, S.; Savoglidis, G.; Fei, Z.; Laurenczy, G.; Alexander, D.T.L.; Yan, N.; Dyson, P.J. A novel platinum nanocatalyst for the oxidation of 5-Hydroxymethylfurfural into 2,5-Furandicarboxylic acid under mild conditions. *J. Catal.* **2014**, *315*, 67–74.
28. Ait Rass, H.; Essayem, N.; Besson, M. Selective aqueous phase oxidation of 5-hydroxymethylfurfural to 2,5-furandicarboxylic acid over Pt/C catalysts: Influence of the base and effect of bismuth promotion. *Green Chem.* **2013**, *15*, 2240–2251.
29. Lolli, A.; Maslova, V.; Bonincontro, D.; Basile, F.; Orтели, S.; Albonetti, S. Selective Oxidation of HMF via Catalytic and Photocatalytic Processes Using Metal-Supported Catalysts. *Molecules* **2018**, *23*, 2792.
30. Qu, H.; Deng, J.; Wang, B.; Ouyang, L.; Tang, Y.; Yu, K.; Lou, L.-L.; Liu, S. Thermoresponsive block copolymer supported Pt nanocatalysts for base-free aerobic oxidation of 5-hydroxymethyl-2-furfural. *Front. Chem. Sci. Eng.* **2021**, *15*, 1514–1523.
31. Cheng, X.; Li, S.; Liu, S.; Xin, Y.; Yang, J.; Chen, B.; Liu, H. Highly efficient catalytic oxidation of 5-hydroxymethylfurfural to 2,5-furandicarboxylic acid using bimetallic Pt–Cu alloy nanoparticles as Catalysts. *Chem. Commun.* **2022**, *58*, 1183–1186.
32. Gui, Z.; Cao, W.; Saravanamurugan, S.; Riisager, A.; Chen, L.; Qi, Z. Efficient Aerobic Oxidation of 5-Hydroxymethylfurfural in Aqueous Media with Au–Pd Supported on Zinc Hydroxycarbonate. *ChemCatChem* **2016**, *8*, 3636–3643.
33. Gao, Z.; Xie, R.; Fan, G.; Yang, L.; Li, F. Highly Efficient and Stable Bimetallic AuPd over La-Doped Ca–Mg–Al Layered Double Hydroxide for Base-Free Aerobic Oxidation of 5-Hydroxymethylfurfural in Water. *ACS Sustain. Chem. Eng.* **2017**, *5*, 5852–5861.
34. Gupta, K.; Rai, R.K.; Dwivedi, A.D.; Singh, S.K. Catalytic Aerial Oxidation of Biomass-Derived Furans to Furan Carboxylic Acids in Water over Bimetallic Nickel–Palladium Alloy Nanoparticles. *ChemCatChem* **2017**, *9*, 2760–2767.

35. Choudhary, H.; Ebitani, K. Hydrotalcite-supported PdPt-catalyzed Aerobic Oxidation of 5-Hydroxymethylfurfural to 2,5-Furandicarboxylic Acid in Water. *Chem. Lett.* **2016**, *45*, 613–615.
36. Wang, Y.; Yu, K.; Lei, D.; Si, W.; Feng, Y.; Lou, L.-L.; Liu, L. Basicity-Tuned Hydrotalcite-Supported Pd Catalysts for Aerobic Oxidation of 5-Hydroxymethyl-2-furfural under Mild Conditions. *ACS Sustain. Chem. Eng.* **2016**, *4*, 4752–4761.
37. Liu, B.; Ren, Y.; Zhang, Z. Aerobic oxidation of 5-hydroxymethylfurfural into 2,5-furandicarboxylic acid in water under mild conditions. *Green Chem.* **2015**, *17*, 1610–1617.
38. Zhang, Z.; Zhen, J.; Liu, B.; Lv, K.; Deng, K. Selective aerobic oxidation of the biomass-derived precursor 5-hydroxymethylfurfural to 2,5-furandicarboxylic acid under mild conditions over a magnetic palladium nanocatalyst. *Green Chem.* **2015**, *17*, 1308–1317.
39. Lolli, A.; Albonetti, S.; Utili, L.; Amadori, R.; Ospitali, F.; Lucarelli, C.; Cavani, F. Insights into the reaction mechanism for 5-hydroxymethylfurfural oxidation to FDCA on bimetallic Pd–Au nanoparticles. *Appl. Catal. A Gen.* **2015**, *504*, 408–419.
40. Siyo, B.; Schneider, M.; Radnik, J.; Pohl, M.-M.; Langer, P.; Steinfeldt, N. Influence of support on the aerobic oxidation of HMF into FDCA over preformed Pd nanoparticle based materials. *Appl. Catal. A Gen.* **2014**, *478*, 107–116.
41. Gupta, N.K.; Nishimura, S.; Takagaki, A.; Ebitani, K. Hydrotalcite-supported gold-nanoparticle-catalyzed highly efficient base-free aqueous oxidation of 5-hydroxymethylfurfural into 2,5-furandicarboxylic acid under atmospheric oxygen pressure. *Green Chem.* **2011**, *13*, 824–827.
42. Davis, S.E.; Zope, B.N.; Davis, R.J. On the mechanism of selective oxidation of 5-hydroxymethylfurfural to 2,5-furandicarboxylic acid over supported Pt and Au catalysts. *Green Chem.* **2012**, *14*, 143–147.
43. Albonetti, S.; Pasini, T.; Lolli, A.; Blosi, M.; Piccinini, M.; Dimitratos, N.; Lopez-Sanchez, J.A.; Morgan, D.J.; Carley, A.F.; Hutchings, G.J.; Cavani, F. Selective oxidation of 5-hydroxymethyl-2-furfural over TiO<sub>2</sub>-supported gold–copper catalysts prepared from preformed nanoparticles: Effect of Au/Cu ratio. *Catal. Today* **2012**, *195*, 120–126.
44. Villa, A.; Schiavoni, M.; Campisi, S.; Veith, G.M.; Prati, L. Pd-modified Au on Carbon as an Effective and Durable Catalyst for the Direct Oxidation of HMF to 2,5-Furandicarboxylic Acid. *ChemSusChem* **2013**, *6*, 609–612.
45. Cai, J.; Ma, H.; Zhang, J.; Song, Q.; Du, Z.; Huang, Y.; Xu, J. Gold Nanoclusters Confined in a Supercage of Y Zeolite for Aerobic Oxidation of HMF under Mild Conditions. *Chem. Eur. J.* **2013**, *19*, 14215–14223.
46. Ardemani, L.; Cibir, G.; Dent, A.J.; Isaacs, M.A.; Kyriakou, G.; Lee, A.F.; Parlett, C.M.A.; Parry, S.A.; Wilson, K. Solid base catalysed 5-HMF oxidation to 2,5-FDCA over Au/hydrotalcites: Fact or fiction? *Chem. Sci.* **2015**, *6*, 4940–4945.
47. Bonincontro, D.; Lolli, A.; Villa, A.; Prati, L.; Dimitratos, N.; Veith, G.M.; Chinchilla, L.E.; Botton, G.A.; Cavani, F.; Albonetti, S. AuPd-nNiO as an effective catalyst for the base-free oxidation of HMF under mild reaction conditions. *Green Chem.* **2019**, *21*, 4090–4099.
48. Uzunidis, G.; Schade, O.; Schild, D.; Grunwaldt, J.-D.; Behrens, S. Design of bimetallic Au/Cu nanoparticles in ionic liquids: Synthesis and catalytic properties in 5-(hydroxymethyl)furfural oxidation. *ChemNanoMat* **2021**, *7*, 1108–1116.
49. Gorbanev, Y.Y.; Kegnæs, S.; Riisager, A. Selective Aerobic Oxidation of 5-Hydroxymethylfurfural in Water Over Solid Ruthenium Hydroxide Catalysts with Magnesium-Based Supports. *Catal. Lett.* **2011**, *141*, 1752–1760.
50. Yi, G.; Teong, S.P.; Zhang, Y. Base-free conversion of 5-hydroxymethylfurfural to 2,5-furandicarboxylic acid over a Ru/C catalyst. *Green Chem.* **2016**, *18*, 979–983.
51. Mishra, D.K.; Lee, H.J.; Kim, J.; Lee, H.-S.; Cho, J.K.; Suh, T.-W.; Yi, Y.; Kim, Y.J. MnCo<sub>2</sub>O<sub>4</sub> spinel supported ruthenium catalyst for air-oxidation of HMF to FDCA under aqueous phase and base-free conditions. *Green Chem.* **2017**, *19*, 1619–1623.
52. Yang, Z.; Qi, W.; Su, R.; He, Z. Selective Synthesis of 2,5-Diformylfuran and 2,5-Furandicarboxylic Acid from 5-Hydroxymethylfurfural and Fructose Catalyzed by Magnetically Separable Catalysts. *Energy Fuels* **2017**, *31*, 533–541.
53. Zheng, L.; Zhao, J.; Du, Z.; Zong, B.; Liu, H. Efficient aerobic oxidation of 5-hydroxymethylfurfural to 2,5-furandicarboxylic acid on Ru/C catalysts. *Sci. China Chem.* **2017**, *60*, 950–957.
54. Zhao, D.; Rodriguez-Padron, D.; Triantafyllidis, K.S.; Wang, Y.; Luque, R.; Len, C. Microwave-Assisted Oxidation of Hydroxymethyl Furfural to Added-Value Compounds over a Ruthenium-Based Catalyst. *ACS Sustain. Chem. Eng.* **2020**, *8*, 3091–3102.
55. Kandasamy, P.; Gogoi, P.; Venugopalan, A.T.; Raja, T. A highly efficient and reusable Ru–NaY catalyst for the base free oxidation of 5-Hydroxymethylfurfural to 2,5-Furandicarboxylic acid. *Catal. Today* **2021**, *375*, 145–154.
56. Su, T.; Liu, Q.; Lü, H.; Alasmay, F.A.; Zhao, D.; Len, C. Selective oxidation of 5-hydroxymethylfurfural to 5-hydroxymethyl-2-furancarboxylic acid using silver oxide supported on calcium carbonate. *Mol. Catal.* **2021**, *502*, 111374.
57. Zhao, D.; Rodriguez-Padron, D.; Luque, R.; Len, C. Insights into the Selective Oxidation of 5-Hydroxymethylfurfural to 5-Hydroxymethyl-2-furancarboxylic Acid Using Silver Oxide. *ACS Sustain. Chem. Eng.* **2020**, *8*, 8486–8495.
58. Celaya, C.A.; Oukhrif, R.; Ait El Had, M.; Abdellaoui, Y.; Abou Oualid, H.; Bourzi, H.; Chahboun, R.; Zhao, D.; Osman, S.M.; Parnar, V.S.; et al. Density functional theory study of the selective oxidation of 5-Hydroxymethylfurfural (HMF) to 5-Hydroxymethyl-2-furancarboxylic acid (HMFCFA) on the Silver oxide surface (001). *Mol. Catal.* **2022**, *519*, 112117.
59. Zope, B.N.; Davis, S.E.; Davis, R.J. Influence of Reaction Conditions on Diacid Formation During Au-Catalyzed Oxidation of Glycerol and Hydroxymethylfurfural. *Top. Catal.* **2012**, *55*, 24–32.
60. Pasini, T.; Piccinini, M.; Blosi, M.; Bonelli, R.; Albonetti, S.; Dimitratos, N.; Lopez-Sanchez, Q.; Kiely, C.J.; Hutchings, G.J.; Cavani, F. Selective oxidation of 5-hydroxymethyl-2-furfural using supported gold–copper nanoparticles. *Green Chem.* **2011**, *13*, 2091–2099.
61. Vuyyuru, R.R.; Strasser, P. Oxidation of biomass derived 5-hydroxymethylfurfural using heterogeneous and electrochemical catalysis. *Catal. Today* **2012**, *195*, 144–154.

62. Albonetti, S.; Lolli, A.; Morandi, V.; Migliori, A.; Lucarelli, C.; Cavani, F. Conversion of 5-hydroxymethylfurfural to 2,5-furandicarboxylic acid over Au-based catalysts: Optimization of active phase and metal-support interaction. *Appl. Catal. B Environ.* **2015**, *163*, 520–530.
63. Subbiah, S.; Simeonov, S.P.; Esperança, J.M.S.S.; Rebelo, L.P.N.; Afonso, C.A.M. Direct transformation of 5-hydroxymethylfurfural to the building blocks 2,5-dihydroxymethylfurfural (DHMF) and 5-hydroxymethyl furanoic acid (HMFA) via Cannizzaro reaction. *Green Chem.* **2013**, *15*, 2849–2853.
64. Kar, S.; Zhou, Q.-Q.; Ben-David, Y.; Milstein, D. Catalytic Furfural/5-Hydroxymethyl Furfural Oxidation to Furoic Acid/Furan-2,5-dicarboxylic Acid with H<sub>2</sub> Production Using Alkaline Water as the Formal Oxidant. *J. Am. Chem. Soc.* **2022**, *144*, 1288–1295.
65. Patil, S.K.R.; Heltzel, J.; Lund, C.R.F. Comparison of Structural Features of Humins Formed Catalytically from Glucose, Fructose, and 5-Hydroxymethylfurfuraldehyde. *Energy Fuels* **2012**, *26*, 5281–5293.
66. Zhang, S.; Zhang, L. A facile and effective method for preparation of 2,5-furandicarboxylic acid via hydrogen peroxide direct oxidation of 5-hydroxymethylfurfural. *Pol. J. Chem. Technol.* **2017**, *19*, 11–16.
67. Partenheimer, W.; Grushin, V.V. Synthesis of 2,5-Diformylfuran and Furan-2,5-Dicarboxylic Acid by Catalytic Air-Oxidation of 5-Hydroxymethylfurfural. Unexpectedly Selective Aerobic Oxidation of Benzyl Alcohol to Benzaldehyde with Metal/Bromide Catalysts. *Adv. Synth. Catal.* **2001**, *343*, 102–111.
68. Zuo, X.; Venkatasubramanian, P.; Busch, D.H.; Subramaniam, B. Optimization of Co/Mn/Br-Catalyzed Oxidation of 5-Hydroxymethylfurfural to Enhance 2,5-Furandicarboxylic Acid Yield and Minimize Substrate Burning. *ACS Sustain. Chem. Eng.* **2016**, *4*, 3659–3668.
69. Zuo, X.; Chaudhari, A.S.; Snavely, K.; Niu, F.; Zhu, H.; Martin, K.J.; Subramaniam, B. Kinetics of Homogeneous 5-Hydroxymethylfurfural Oxidation to 2,5-Furandicarboxylic Acid with Co/Mn/Br Catalyst. *AIChE J.* **2017**, *63*, 162–171.
70. Chen, S.; Guo, X.; Ban, H.; Pan, T.; Zheng, L.; Cheng, Y.; Wang, L.; Li, X. Reaction Mechanism and Kinetics of the Liquid-Phase Oxidation of 5-Hydroxymethylfurfural to 2,5-Furandicarboxylic Acid. *Ind. Eng. Chem. Res.* **2021**, *60*, 16887–16898.
71. Han, X.; Li, C.; Liu, X.; Xia, Q.; Wang, Y. Selective oxidation of 5-hydroxymethylfurfural to 2,5-furandicarboxylic acid over MnO<sub>x</sub>-CeO<sub>2</sub> composite catalysts. *Green Chem.* **2017**, *19*, 996–1004.
72. Fu, M.; Yang, W.; Yang, C.; Zhang, Y.; Shen, C. Mechanistic insights into CoO<sub>x</sub>-Ag/CeO<sub>2</sub> catalysts for the aerobic oxidation of 5-hydroxymethylfurfural to 2,5-furandicarboxylic acid. *Catal. Sci. Technol.* **2022**, *12*, 116–123.
73. Wang, S.; Zhang, Z.; Liu, B. Catalytic Conversion of Fructose and 5-Hydroxymethylfurfural into 2,5-Furandicarboxylic Acid over a Recyclable Fe<sub>3</sub>O<sub>4</sub>-CoO<sub>x</sub> Magnetite Nanocatalyst. *ACS Sustain. Chem. Eng.* **2015**, *3*, 406–412.
74. Jain, A.; Jonnalagadda, S.C.; Ramanujachary, K.V.; Mugweru, A. Selective oxidation of 5-hydroxymethyl-2-furfural to furan-2,5-dicarboxylic acid over spinel mixed metal oxide catalyst. *Catal. Commun.* **2015**, *58*, 179–182.
75. Gawade, A.B.; Nakhate, A.V.; Yadav, G.D. Selective synthesis of 2, 5-furandicarboxylic acid by oxidation of 5-hydroxymethylfurfural over MnFe<sub>2</sub>O<sub>4</sub> catalyst. *Catal. Today* **2018**, *309*, 119–125.
76. Wang, F.; Lai, J.; Liu, Z.; Wen, S.; Liu, X. Copper-manganese oxide for highly selective oxidation of 5-hydroxymethylfurfural to bio-monomer 2, 5-furandicarboxylic acid. *Biomass Convers. Biorefin.* **2022**, *in press*.
77. Gao, L.; Deng, K.; Zheng, J.; Liu, B.; Zhang, Z. Efficient oxidation of biomass derived 5-hydroxymethylfurfural into 2,5-furandicarboxylic acid catalyzed by Merrifield resin supported cobalt porphyrin. *Chem. Eng. J.* **2015**, *270*, 444–449.
78. Vandarkuzhali, S.A.A.; Karthikeyan, G.; Pachamuthu, M.P. Efficient oxidation of 5-Hydroxymethylfurfural to 2,5-furandicarboxylic acid over FeNPs@NH<sub>2</sub>-SBA-15 catalyst in water. *Mol. Catal.* **2021**, *516*, 111951.
79. Saha, B.; Gupta, D.; Abu-Omar, M.M.; Modak, A.; Bhaumik, A. Porphyrin-based porous organic polymer-supported iron(III) catalyst for efficient aerobic oxidation of 5-hydroxymethyl-furfural into 2,5-furandicarboxylic acid. *J. Catal.* **2013**, *299*, 316–320.
80. Yang, C.; Li, X.; Zhang, Z.; Lv, B.; Li, J.; Liu, Z.; Zhu, W.; Tao, F.; Lv, G.; Yang, Y. High efficient catalytic oxidation of 5-hydroxymethylfurfural into 2,5-furandicarboxylic acid under benign conditions with nitrogen-doped graphene encapsulated Cu nanoparticles. *J. Energy Chem.* **2010**, *50*, 96–105.
81. Cheng, F.; Guo, D.; Lai, J.; Long, M.; Zhao, W.; Liu, X.; Yin, D. Efficient base-free oxidation of 5-hydroxymethylfurfural to 2,5-furandicarboxylic acid over copper-doped manganese oxide nanorods with tert-butanol as solvent. *Front. Chem. Sci. Eng.* **2021**, *15*, 960–968.
82. Zhang, Z.; Liu, B.; Lv, K.; Sun, J.; Deng, K. Aerobic oxidation of biomass derived 5-hydroxymethylfurfural into 5-hydroxymethyl-2-furancarboxylic acid catalyzed by a montmorillonite K-10 clay immobilized molybdenum acetylacetonate complex. *Green Chem.* **2014**, *16*, 2762–2770.
83. Neatu, F.; Marina, R.S.; Florea, M.; Petrea, N.; Pavel, O.D.; Parvulescu, V.I. Selective oxidation of 5-hydroxymethyl furfural over non-precious metal heterogeneous catalysts. *Appl. Catal. B Environ.* **2016**, *180*, 751–757.
84. Hayashi, E.; Komanoya, T.; Kamata, K.; Hara, M. Heterogeneously-Catalyzed Aerobic Oxidation of 5-Hydroxymethylfurfural to 2,5-Furandicarboxylic Acid with MnO<sub>2</sub>. *ChemSusChem* **2017**, *10*, 654–658.
85. Grabowski, G.; Lewkowski, J.; Skowronski, R. The electrochemical oxidation of 5-hydroxymethylfurfural with the nickel oxide/hydroxide electrode. *Electrochim. Acta* **1991**, *36*, 1995.
86. Zhang, J.; Yu, P.; Zeng, G.; Bao, F.; Yuan, Y.; Huang, H. Boosting HMF oxidation performance via decorating ultrathin nickel hydroxide nanosheets with amorphous copper hydroxide islands. *J. Mater. Chem. A* **2021**, *9*, 9685–9691.
87. Su, T.; Zhao, D.; Wang, Y.; Lu, H.; Varma, R.S.; Len, C. Innovative Protocols in the Catalytic Oxidation of 5-Hydroxymethylfurfural. *ChemSusChem* **2021**, *14*, 266–280.

88. Wei, P.; Bieringer, M.; Cranswick, L.M.D.; Petric, A. In situ high-temperature X-ray and neutron diffraction of Cu–Mn oxide phases. *J. Mat. Sci.* **2010**, *45*, 1056–1064.
89. Vandenberghe, R.E.; Robbrechr, G.G.; Brabers, V.A.M. Structure and ionic configuration of oxidic copper-manganese spinels ( $\text{Cu}_x\text{Mn}_{3-x}\text{O}_4$ ). *Phys. Stat. Sol. A* **1976**, *34*, 583–592.
90. Martin, B.E.; Petric, A. Electrical properties of copper–manganese spinel solutions and their cation valence and cation distribution. *J. Phys. Chem. Solids* **2007**, *68*, 2262–2270.
91. Maunders, C.; Martin, B.E.; Wei, P.; Petric, A.; Botton, G.A. Investigation of the electronic structure of the cubic spinel  $\text{Cu}_{1.2}\text{Mn}_{1.8}\text{O}_4$  using electron energy loss spectroscopy. *Solid State Ion.* **2008**, *179*, 718–724.
92. Broemme, A.D.D.; Brabers, V.A.M. Preparation and Properties of Copper and Manganese Containing Mixed Oxide. *Solid State Ion.* **1985**, *16*, 171–178.
93. Lavina, B.; Salviulo, G.; Della Giusta, A. Cation distribution and structure modelling of spinel solid solutions. *Phys. Chem. Miner.* **2002**, *29*, 10–18.
94. Vozniuk, O.; Bazzo, C.; Albonetti, S.; Tanchoux, N.; Bosselet, F.; Millet, J.-M.; Di Renzo, F.; Cavani, F. Structural Changes of Binary/Ternary Spinel Oxides During Ethanol Anaerobic Decomposition. *ChemCatChem* **2017**, *9*, 2219–2230.
95. Cornell, R.M.; Schwertmann, U. *The Iron Oxides. Structure, Properties, Reactions, Occurrences and Uses*; Wiley-VCH: Weinheim, Germany, 2003; pp. 158–159.
96. Cedeño-Mattei, Y.; Perales-Pérez, O.; Uwakweh, O.N.C. Synthesis of high-coercivity non-stoichiometric cobalt ferrite nanocrystals: Structural and magnetic characterization. *Mat. Chem. Phys.* **2012**, *132*, 999–1006.
97. Murray, P.J.; Linnett, J.W. Cation Distribution in the Spinel  $\text{Co}_x\text{Fe}_{3-x}\text{O}_4$ . *J. Phys. Chem. Solids* **1976**, *37*, 1041–1042.
98. Li, K.Z.; Haneda, M.; Ozawa, M. The synthesis of iron oxides with different phases or exposure crystal planes and their catalytic property for propene oxidation. *Adv. Mat. Res.* **2012**, *463–464*, 189–193.
99. Tiernan, M.J.; Barnes, P.A.; Parkes, G.M.B. Reduction of Iron Oxide Catalysts: The Investigation of Kinetic Parameters Using Rate Perturbation and Linear Heating Thermoanalytical Techniques. *J. Phys. Chem. B* **2001**, *105*, 220–228.
100. Zhu, J.; Andersson, S.L.T. Reaction Network and Kinetics for the Catalytic Oxidation of Toluene over  $\text{V}_2\text{O}_5$ . *J. Catal.* **1990**, *126*, 92–100.
101. Horvat, J.; Klaić, B.; Metelko, B.; Sunjic, V. Mechanism of levulinic acid formation. *Tetrahedron Lett.* **1985**, *26*, 2111–2114.
102. van Zandvoort, I.; Koers, E.J.; Weingarth, M.; Bruijninx, P.C.A.; Baldus, M.; Weckhuysen, B.M. Structural characterization of  $^{13}\text{C}$ -enriched humins and alkali-treated  $^{13}\text{C}$  humins by 2D solid-state NMR. *Green Chem.* **2015**, *17*, 4383–4392.
103. Nichela, D.A.; Berkovic, A.M.; Costante, M.R.; Juliarena, M.P.; Einschlag, F.S.G. Nitrobenzene degradation in Fenton-like systems using Cu(II) as catalyst. Comparison between Cu(II)- and Fe(III)-based systems. *Chem. Eng. J.* **2013**, *228*, 1148–1157.
104. Shen, Y.; Zhang, Z.; Xiao, K. Evaluation of cobalt oxide, copper oxide and their solid solutions as heterogeneous catalysts for Fenton-degradation of dye pollutants. *RSC Adv.* **2015**, *5*, 91846–91854.
105. Qi, L.; Qi, X.; Wang, L.; Feng, L.; Lu, S. Decomposition of tert-butyl hydroperoxide into tert-butyl alcohol and  $\text{O}_2$  catalyzed by birnessite-type manganese oxides: Kinetics and activity. *Catal. Commun.* **2014**, *49*, 6–9.
106. Debnath, B.; Roy, A.S.; Kapri, S.; Bhattacharyya, S. Efficient Dye Degradation Catalyzed by Manganese Oxide Nanoparticles and the Role of Cation Valence. *ChemistrySelect* **2016**, *1*, 4265–4273.
107. Weng, Z.; Li, J.; Weng, Y.; Feng, M.; Zhuang, Z.; Yu, Y. Surfactant-free porous nano- $\text{Mn}_3\text{O}_4$  as a recyclable Fenton-like reagent that can rapidly scavenge phenolics without  $\text{H}_2\text{O}_2$ . *J. Mater. Chem. A* **2017**, *5*, 15650–15660.
108. Lin, Z.-R.; Zhao, L.; Dong, Y.-H. Effects of low molecular weight organic acids and fulvic acid on 2,4,4'-trichlorobiphenyl degradation and hydroxyl radical formation in a goethite-catalyzed Fenton-like reaction. *Chem. Eng. J.* **2017**, *326*, 201–209.
109. Araujo, F.V.F.; Yokoyama, L.; Teixeira, L.A.C.; Campos, J.C. Heterogeneous Fenton process using the mineral hematite for the discoloration of a reactive dye solution. *Braz. J. Chem. Eng.* **2011**, *28*, 605–616.
110. Busca, G. The surface acidity of solid oxides and its characterization by IR spectroscopic methods. An attempt at systematization. *Phys. Chem. Chem. Phys.* **1999**, *1*, 723–736.
111. Biswas, S.; Dutta, B.; Mannodi-Kanakithodi, A.; Clarke, R.; Song, W.; Ramprasad, R.; Suib, S.L. Heterogeneous mesoporous manganese/cobalt oxide catalysts for selective oxidation of 5-hydroxymethylfurfural to 2,5-diformylfuran. *Chem. Commun.* **2017**, *53*, 11751–11754.
112. Hanna, K.; Kone, T.; Medjahdi, G. Synthesis of the mixed oxides of iron and quartz and their catalytic activities for the Fenton-like oxidation. *Catal. Commun.* **2008**, *9*, 955–959.
113. Voinov, M.A.; Sosa Pagan, J.O.; Morrison, E.; Smirnova, T.I.; Smirnov, A.I. Surface-Mediated Production of Hydroxyl Radicals as a Mechanism of Iron Oxide Nanoparticle Biototoxicity. *J. Am. Chem. Soc.* **2011**, *133*, 35–41.
114. Chen, Z.; Yin, J.J.; Zhou, Y.T.; Zhang, Y.; Song, L.; Song, M.; Hu, S.; Gu, N. Dual Enzyme-like Activities of Iron Oxide Nanoparticles and Their Implication for Diminishing Cytotoxicity. *ACS Nano* **2012**, *6*, 4001–4012.
115. Zasada, F.; Piskorz, W.; Janas, J.; Grybos, J.; Indyka, P.; Sojka, Z. Reactive Oxygen Species on the (100) Facet of Cobalt Spinel Nanocatalyst and their Relevance in  $^{16}\text{O}_2/^{18}\text{O}_2$  Isotopic Exchange,  $\text{deN}_2\text{O}$ , and  $\text{deCH}_4$  Processes. A Theoretical and Experimental Account. *ACS Catal.* **2015**, *5*, 6879–6892.
116. Zasada, F.; Janas, J.; Piskorz, W.; Sojka, Z. Surface oxygen dynamics and  $\text{H}_2$  oxidation on cobalt spinel surface probed by  $^{18}\text{O}/^{16}\text{O}$  isotopic exchange and accounted for by DFT molecular modeling: Facile interfacial oxygen atoms flipping through transient peroxy intermediate. *Res. Chem. Intermed.* **2017**, *43*, 2865–2880.

117. Brazdil, J.F. Scheelite: A versatile structural template for selective alkene oxidation catalysts. *Catal. Sci. Technol.* **2015**, *5*, 3452–3458.
118. Massa, M.; Häggblad, R.; Andersson, A. Cation Vacant  $\text{Fe}_{3-x}\text{V}_x\text{O}_4$  Spinel-Type Catalysts for the Oxidation of Methanol to Formaldehyde. *Top. Catal.* **2011**, *54*, 685–697.
119. Reddy, A.S.; Gopinath, C.S.; Chilukuri, S. Selective ortho-methylation of phenol with methanol over copper manganese mixed-oxide spinel catalysts. *J. Catal.* **2006**, *243*, 278–291.
120. Gurralla, L.; Nagpure, A.S.; Gurav, H.R.; Chilukuri, S. Spinel-Type Mixed Oxides for Stable and Selective Partial Oxidation of Benzyl Alcohol. *ChemistrySelect* **2018**, *3*, 3751–3761.
121. Tirsoaga, A.; El Fergani, M.; Nuns, N.; Simon, P.; Granger, P.; Parvulescu, V.; Comana, S.M. Multifunctional nanocomposites with non-precious metals and magnetic core for 5-HMF oxidation to FDCA. *Appl. Catal. A Gen.* **2020**, *278*, 119309.
122. Girisuta, B.; Janssen, L.P.B.M.; Heeres, H.J. A kinetic study on the decomposition of 5-hydroxymethylfurfural into levulinic acid. *Green Chem.* **2006**, *8*, 701–709.
123. van Zandvoort, I.; Wang, Y.; Rasrendra, C.B.; van Eck, E.R.H.; Bruijninx, P.C.A.; Heeres, H.J.; Weckhuysen, B.M. Formation, Molecular Structure, and Morphology of Humins in Biomass Conversion: Influence of Feedstock and Processing Conditions. *ChemSusChem* **2013**, *6*, 1745–1758.
124. Pipitone, G.; Zoppi, G.; Frattini, A.; Bocchini, S.; Pirone, R.; Bensaid, S. Aqueous phase reforming of sugar-based biorefinery streams: From the simplicity of model compounds to the complexity of real feeds. *Catal. Today* **2020**, *345*, 267–279.
125. Dong, X.; Wang, X.; Song, H.; Zhang, Y.; Yuan, A.; Guo, Z.; Wang, Q.; Yang, F. Enabling Efficient Aerobic 5-Hydroxymethylfurfural Oxidation to 2,5-Furandicarboxylic Acid in Water by Interfacial Engineering Reinforced Cu–Mn Oxides Hollow Nanofiber. *ChemSusChem* **2022**, *15*, e202200076.
126. Megías-Sayago, C.; Chabarova, K.; Penkova, A.; Lolli, A.; Ivanova, S.; Albonetti, S.; Cavani, F.; Odriozola, J.A. Understanding the Role of the Acid Sites in 5-Hydroxymethylfurfural Oxidation to 2,5-Furandicarboxylic Acid Reaction over Gold Catalysts: Surface Investigation on  $\text{Ce}_x\text{Zr}_{1-x}\text{O}_2$  Compounds. *ACS Catal.* **2018**, *8*, 11154–11164.
127. Sreekumar, K.; Sugunan, S. Ferrospinel based on Co and Ni prepared via a low temperature route as efficient catalysts for the selective synthesis of o-cresol and 2,6-xyleneol from phenol and methanol. *J. Mol. Catal. A Gen.* **2002**, *185*, 259–268.
128. Ballarini, N.; Cavani, F.; Passeri, S.; Pesaresi, L.; Lee, A.F.; Wilson, K. Phenol methylation over nanoparticulate  $\text{CoFe}_2\text{O}_4$  inverse spinel catalysts: The effect of morphology on catalytic performance. *Appl. Catal. A Gen.* **2009**, *366*, 184–192.
129. O'Neill, H.S.C.; Navrotsky, A. Cation distributions and thermodynamic properties of binary spinel solid solutions. *Am. Miner.* **1983**, *68*, 181–194.
130. Ferreira, T.A.S.; Waerenborgh, J.C.; Mendonça, M.H.R.M.; Nunes, M.R.; Costa, F.M. Structural and morphological characterization of  $\text{FeCo}_2\text{O}_4$  and  $\text{CoFe}_2\text{O}_4$  spinels prepared by a coprecipitation method. *Solid State Sci.* **2003**, *5*, 383–392.
131. Hill, R.J.; Craig, J.R.; Gibbs, G.V. Systematics of the Spinel Structure Type. *Phys. Chem. Miner.* **1979**, *4*, 317–339.
132. Ustinov, E.A.; Do, D.D.; Jaroniec, M. Equilibrium Adsorption in Cylindrical Mesopores: A Modified Broekhoff and de Boer Theory versus Density Functional Theory. *J. Phys. Chem. B* **2005**, *109*, 1947–1958.
133. Payne, S.M.; Kerton, F.M. Solubility of bio-sourced feedstocks in 'green' solvents. *Green Chem.* **2010**, *12*, 1648–1653.